2010

# CONSTITUENTS OF SEA SURFACE HEIGHT VARIABILITY IN DRAKE PASSAGE

Amy Lynn Cutting
*University of Rhode Island*

**Library Rights Statement**

In presenting the thesis, Constituents of Sea Surface Height Variability in Drake Passage, in partial fulfillment of the requirements for an advanced degree at the University of Rhode Island, I agree that the Library shall make it freely available for inspection. I further agree that permission for copying, as provided for by the Copyright Law of the United States (Title 17, U.S. Code), of this thesis for scholarly purposes may be granted by the Librarian. It is understood that any copying or publication of this thesis for financial gain shall not be allowed without my written permission.

I hereby grant permission to the University of Rhode Island Library to use my thesis for scholarly purposes.

_____

Amy Lynn Cutting

_____

Date

# CONSTITUENTS OF SEA SURFACE HEIGHT VARIABILITY IN DRAKE PASSAGE

BY

AMY LYNN CUTTING

A THESIS SUBMITTED IN PARTIAL FULFILLMENT OF THE

REQUIREMENTS FOR THE DEGREE OF

MASTER OF SCIENCE

IN

OCEANOGRAPHY

UNIVERSITY OF RHODE ISLAND

2010

MASTER OF SCIENCE THESIS

OF

AMY LYNN CUTTING

APPROVED:

Thesis Committee:

Major Professor _____

_____

_____

_____

DEAN OF THE GRADUATE SCHOOL

UNIVERSITY OF RHODE ISLAND

2010

**ABSTRACT**

As part of the International Polar Year, cDrake, an array of current and pressure recording inverted echo sounders (CPIES), was deployed in Drake Passage in November 2007. The array will be in place for four years and the data collected annually by acoustic telemetry. The CPIES array consists of a transport line, 22 CPIES that span Drake Passage and a local dynamics array, a grid of 21 CPIES centered on the surface eddy kinetic energy maximum in the passage. Acoustic round-trip travel time and bottom pressure anomaly are used to compute sea surface height anomaly (SSHA) at each site. Round-trip travel time measurements are converted to geopotential using historical hydrography. Geopotential is divided by gravity to determine the steric component of SSHA. The mass-loading component of SSHA is computed by dividing the bottom pressure anomaly by the product of density and local gravity. The mass-loading and steric SSHA components are uncorrelated, except in the eastern local dynamics array, at three sites where strong deep cyclone formation associated with the meandering Polar Front lead to correlation coefficients greater than 0.4. Relative contributions of steric and mass-loading components vary along the transport line. North of 57°S, steric SSHA variance exceeds 60% of the total SSHA variance. South of 59°S, the mass-loading SSHA variance exceeds 40% of the total SSHA variance and in places reaches 65% of the total variance.

The CPIES-derived SSHA is compared with SSHA from an along-track and a merged and mapped satellite SSHA product. Correlations with both products varied widely depending on the variability in the records, but most were above 0.9 and statistically significant. Notable exceptions occur along the southern end of the transport line, where correlations dip to 0.2-0.7. The Nyquist frequency of the Topex/Poseidon, Jason-1 and Jason-2 satellite repeat is 1/20 cycles-per-day. Signals with frequencies higher than this will get aliased by the altimeter sampling. In cDrake, the aliased variance exceeds 20% of the total signal variance in the middle of the dynamics array and on the southern

end of the transport line. There is potential of aliasing of both the steric and mass-loading SSHA in Drake Passage. Analysis of the SSHA records with frequencies higher than 1/20 cpd from recovered cDrake instruments shows no correlation with the high-frequency barotropic model output used to correct altimetry measurements for high frequency signals. The model underestimates the signals throughout the cDrake array. Aliasing of these signals will continue unless a better correction for the mass-loading variance is found and a steric high-frequency correction is developed.

**ACKNOWLEDGEMENTS**

This thesis would not have been possible without the guidance, motivation, patience, and enthusiasm of Kathy Donohue. She is a wonderful advisor, teacher, and friend. I am also grateful to Randy Watts and Gopu Potty for their knowledge and input to this work, and for serving as committee members. Thanks to Jan Northby for serving as the committee chairperson.

I am indebted to my many colleagues who supported both me and the cDrake project, especially Karen Tracey and Teri Chereskin. Erran Sousa, Gerry Chaplin, and the staff of the Equipment Development Laboratory ensured working instrumentation and successful recovery of data. Without these people, along with the other cDrake cruise participants, Raytheon Polar Services, the captains and crew of the RVIB Nathaniel B. Palmer, and the National Science Foundation Office of Polar Programs, this work would not be possible.

I am most grateful for the support of my husband, family and friends for their love and encouragement.

## PREFACE

Rather than using the traditional division of the thesis into chapters, this thesis is written in "manuscript" style. The main text is written in a manner appropriate for submission to a scientific journal.

Manuscript 1

# Constituents of Sea Surface Height Variability in Drake Passage

by

Amy L. Cutting[1], Kathleen A. Donohue[1], and D. Randolph Watts[1]

formatted for submission to the Journal of Geophysical Research - Oceans

[1]Graduate School of Oceanography, University of Rhode Island, Narragansett, Rhode Island, USA.

Corresponding author: afearing@gso.uri.edu

**TABLE OF CONTENTS**

## LIST OF TABLES

## LIST OF FIGURES

# MANUSCRIPT 1

## Constituents of Sea Surface Height Variability in Drake Passage

### 1.1 Introduction

The Antarctic Circumpolar Current (ACC) is a unique oceanic feature in many respects. It is the only zonally unbounded current system in the world, and is comprised of three eastward flowing circumpolar jets. From north to south they are the Subantarctic Front (SAF), the Polar Front (PF), and the Southern Antarctic Circumpolar Current Front (SACCF) [*Orsi et al.*, 1995]. The ACC connects the three major ocean basins, and because of these connections, it permits a global meridional overturning circulation. The jets are deep reaching and are steered in many areas by topography [*Gille*, 2002]. The ACC is driven by the band of westerly winds at the same latitude in the atmosphere. Ekman transport from the wind forcing helps transform and export water masses that contribute to the overturning circulation [*Speer et al.*, 2000].

Eddies play a significant role in transporting heat in the Southern Ocean. Heating of the atmosphere is strongest at the equator and weakest at the poles. In order to keep the atmospheric temperatures from becoming extreme, the ocean must redistribute the excess heat in the equatorial regions poleward. In the southern hemisphere, the ACC acts as a boundary, keeping the Antarctic continent isolated. Because of this separation, eddies must be responsible for the heat flux to the higher latitudes to compensate this lack of atmospheric heating [*deSzoeke and Levine*, 1981].

The Southern Ocean has been shown to be especially susceptible to climate change. The atmospheric westerly winds over the Southern Ocean have increased wind stress over the ACC [*Yang et al.*, 2007]. In addition to this increased forcing, float and hydrographic observations over the past fifty years have shown increasing temperatures [*Gille*, 2008]. While coarse resolution numerical models such as the one used by *Gnanadesikan and*

*Hallberg* [2000] predict that the warming is accompanied by an increase in transport throughout the ACC, observations have shown no change to the tilt of isopycnals across the current, keeping the transport relatively stable [*Böning et al.*, 2008]. There have been two suggested mechanisms for the warming in the Southern Ocean. The first mechanism is a poleward shift of the ACC [*Gille*, 2008]. The second is an increased heat flux. *Hogg et al.* [2007] used an eddy resolving quasi-geostrophic model to study how increasing wind stress could lead to an increase in heat flux. With the high resolution of their model, they were able to see a first response in the form of increased Ekman transport in the surface layers, which resulted in cooling. Ultimately, the model reproduced ocean warming similar to the observation over the past 50 years because the increase in eddy activity led to a net poleward heat flux. While there is lingering debate over the dynamic mechanisms at work in the Southern Ocean, observations have shown that the ACC is undergoing major changes.

Despite being the largest current system in the world, the transport of the ACC has not been accurately monitored, due in part to its size. Geographically, there are three horizontal chokepoints of the ACC between Antarctica and South America, Africa, and Australia. The smallest of these is created by South America, in Drake Passage. For this reason, many experiments have taken place there in an attempt to monitor the ACC. The last major field experiment that aimed to measure total transport was in the 1970s. The first dynamic response and kinematic experiment used an array of current meters and a pair of bottom pressure gauges to measure transport in Drake Passage. The transport was estimated as 134±13 Sv [*Whitworth*, 1983; *Whitworth and Peterson*, 1985].

As part of the International Polar Year, the cDrake project is designed to study the ACC using an array of current and pressure recording inverted echo sounders (CPIES) and current-meter moorings (figure 1.1). The CPIES array consists of a transport line comprising a line of CPIES that span Drake Passage (22 CPIES), and a local dynamics array comprising a grid of 21 CPIES centered on the eddy kinetic energy maximum in

the passage around 57°W 63°S (figure 1.1). cDrake will quantify ACC transport and dynamics. The transport line will determine horizontal and vertical structure of the time-varying transport. The local dynamics array exists between the Subantarctic Front and Polar Front within the region of maximum surface variability and will describe the mesoscale eddy field. The full data set will also provide metrics to assess the skill of model simulations. Ultimately, the cDrake project aims to provide guidance for future monitoring and studies of the ACC.

Satellite altimetry has been utilized for the past 18 years to study the ocean with mesoscale resolution and altimetry and other remotely sensed observations are likely to be part of future monitoring of the ACC, as well as the global ocean. Altimeters provide sea surface height measurements. New satellite missions aim at measuring temporal changes in gravity, which provide estimates of changes in total water storage or mass. There is community interest to combine these measurements in order to decompose the sea surface height into its two constituents, steric and mass-loading [*Jayne et al.*, 2003; *Bingham and Hughes*, 2008]. The benefit of this decomposition is a better understanding of the ocean's variability. For example, low-frequency ACC variability may arise from changes in heat content while the ACC's high-frequency response to changes in atmospheric forcing may be primarily mass-loading. In addition, uncertainties exist regarding the potential aliasing of high-frequency ACC variability due to the sampling interval of contemporary satellite missions. It is important to know the strengths and weaknesses of the present and proposed satellite altimeters to better design comprehensive monitoring systems in the future.

In the next section, details of the cDrake dataset and processing schemes are provided, as well as a description of the altimetric products utilized in the analysis. Section 1.3 shows the SSHA results as a function of time, space, and frequency. Steric and mass-loading constituents of SSHA vary with latitude along the cDrake transport line, with highest variance in the local dynamics array at frequencies longer than 1/20 cycles per day. There is significant energy at frequencies below 1/20 cycles per day which are

aliased to frequencies measured by the altimeter. In section 1.5, comparisons are made between the cDrake data and satellite altimetry data from AVISO (Archiving, Validation and Interpretation of Satellite Oceanographic data). This paper will show that along-track and merged, gridded products correlate best with CPIES measurements at sites that have high variance, and in general correlations with the merged product are higher. Analyses of high-frequency signals from the CPIES instruments reveal that in Drake Passage the high-frequency correction applied to the altimetry measurements is not adequate to prevent aliasing of mass-loading SSHA signals and furthermore a correction to steric SSHA signals would be necessary to eliminate aliased high-frequency energy.

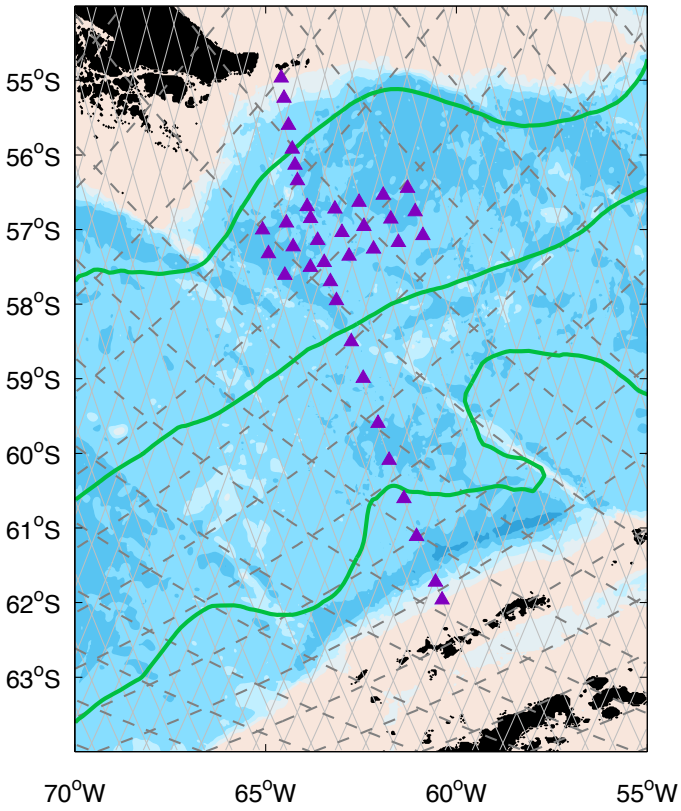


Figure 1.1: cDrake CPIES (purple triangles) span Drake Passage. Topography (*Smith and Sandwell* [1997], version 6.2) color-shaded every 1000 m depth. Land is shown as black. Two satellite altimeters operated during the cDrake measurement time period discussed in this study (Nov. 2007 through Dec. 2009): ERS (light gray) and Jason-2 (dashed dark gray). Mean positions of three major ACC fronts inferred by altimetry data as in *Lenn et al.* [2008] shown with thick green lines.

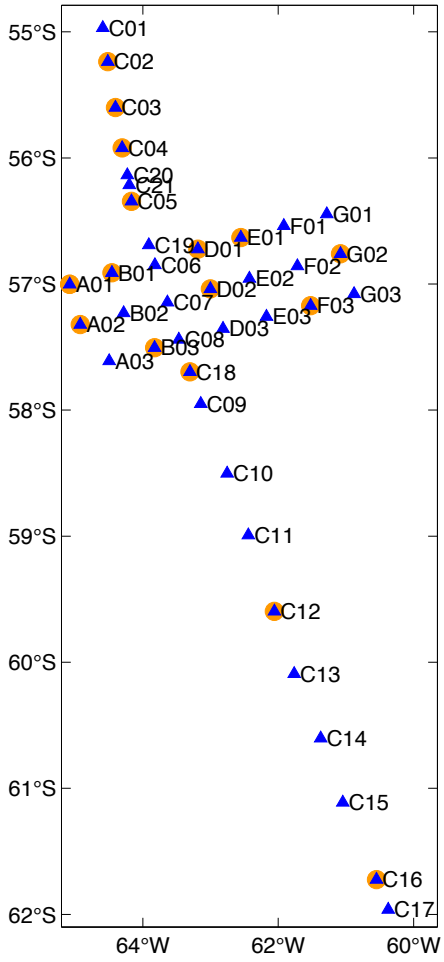


Figure 1.2: Sites with recovered instruments (orange circles) within the cDrake CPIES array (blue triangles).

## 1.2 Data and Methods

### 1.2.1 The cDrake Array

cDrake CPIES measured round-trip travel time ($\tau$), pressure, and bottom current. Techniques have been developed that use $\tau$ as a proxy for temperature, salinity, and geopotential (T, S, and $\phi$) in the ACC [*Watts et al.*, 2001] as well as in the cDrake region [*Sun and Watts*, 2001]. Briefly, a look-up table is created from historical hydrography that relates a predetermined $\tau$ index to hydrographic profiles. This is the so-called gravest empirical mode (GEM). Measured $\tau$ values are converted to a $\tau$ index and with the GEM, vertical profiles of T and S can be estimated at any CPIES site. Due to inherent variability in the upper ocean, there is some error introduced in the GEM and $\tau$ measurements. Part of this variability is a seasonal cycle in T and S, and therefore $\tau$. By quantifying and removing the seasonal signal from the GEM and $\tau$ measurements, the errors from the upper ocean variability can be reduced. The following sections outline the methods used to construct a seasonal cycle, create cDrake GEMs, and process $\tau$ and bottom-pressure data as well as introduce the satellite altimetry products.

### 1.2.2 Seasonal-Cycle Construction

Seasonal variations in heat and freshwater fluxes occur in the upper-water column [*Watts et al.*, 2001]. Due to these changes, there is more variability and therefore error in the upper 150 meters of the GEM. To reduce the scatter, the seasonal correction to T, S, and $\tau$ as a function of generic yearday was constructed and removed from hydrographic casts as follows.

Conductivity, temperature, and depth (CTD) casts in Drake Passage during austral winter were sparse, so to gain better resolution for all seasons, expendable conductivity, temperature and depth (XCTD) casts were used to examine the seasonal cycle in the upper ocean. XCTD data were made available by Janet Sprintall and are part of the Scripps High Resolution XBT program in Drake Passage. There are at least 10 casts in each month, and more than 20 during each of the austral winter months. The distribution of the XCTD casts geographically, by month, and by year is shown in figure 1.3.

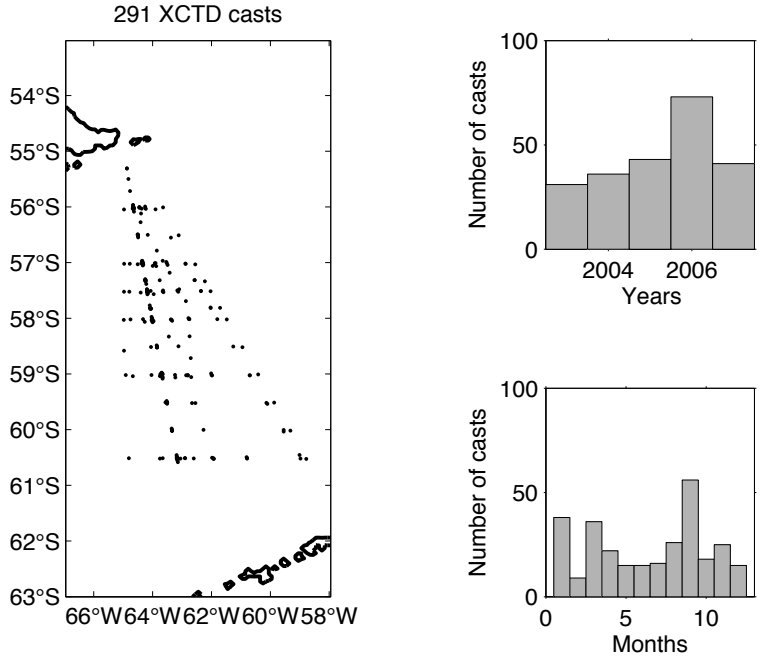


Figure 1.3: Left panel: Map of XCTD casts used to construct the seasonal cycles. Right panels: Histograms of cast year (top) and month (bottom).

The first step computed the $\tau$ value of each cast between the shallowest level that

had no seasonal signal (150 dbar) and the deepest level common to all casts (1000 dbar) as

$$\tau_{150-1000} = \int_{150}^{1000} \frac{2}{\rho g c} dp, \tag{1.1}$$

where $g$ is gravity (9.8 m $s^{-2}$), c is the speed of sound, $\rho$ is the density of seawater, and p is pressure. Upper-ocean $\tau_{0-150}$, temperature or salinity at a chosen pressure level was plotted versus $\tau_{150-1000}$. A spline was fit (upper panel of each pair in figures 1.4 and 1.5) and then the residuals were computed. The residual was then sorted by generic yearday (lower panel of each pair in figures 1.4 and 1.5). This made apparent the seasonal signal. A 3-month running mean was computed to form a smoothed seasonal cycle for $\tau$, temperature or salinity. The $\tau$ seasonal signal range was 0.9 ms in the upper 150 meters. The seasonal cycle was mainly confined to the upper hundred meters. The maximum temperature correction range was 2.2°C at the surface. No correction was made below 150 m depth. The salinity signal has a maximum value at 40 m, and has a range of 0.08 PSU. Slight smoothing of the 3-month running mean resulted in the seasonal signal that was removed from the hydrographic data or CPIES $\tau$ measurements (figure 1.6).

In the Subantarctic flux and dynamics experiment (SAFDE), the seasonal signal of the Subantarctic Front south of Australia was quantified [*Watts et al.*, 2001]. Table 1.1 shows the values in SAFDE and cDrake for $\tau$, T, and S. In SAFDE, the seasonal cycle extended to 200 m, slightly deeper than the cDrake seasonal correction. In addition, the range in temperature correction at the surface was slightly lower and the salinity signal was stronger in SAFDE.

The temporal and depth patterns of the temperature and salinity cycles in cDrake were very similar to those seen in SAFDE. The temperature cycle showed warming in austral spring and cooling in fall in the upper 50 dbar. There was a lag of up to a month in the lower 100 dbar. The lag was smaller in the winter than the summer, as it was in SAFDE. The small lag in winter can be attributed to increased winds cooling surface waters quickly, causing buoyancy destabilization and therefore convective overturning mixing the cold waters down through the water column quickly. The summer mixed layer

was thinner due to lighter winds, and the heating at the surface provided a stabilizing force, making the temperature transfer occur more slowly [*Watts et al.*, 2001].

The lag in the salinity seasonal cycle with depth was much more pronounced than the lag in the temperature signal. The cDrake and SAFDE signals both show the signal around 100 - 150 dbar having an offset of approximately 4 months. This makes the minimum and maximum salinity signals at 125 dbar in cDrake in phase with the temperature correction at the surface. *Watts et al.* [2001] explain this signal in terms of the excess precipitation year-round combined with the mixed-layer cycles. Throughout the summer, the excess freshwater decreases the salinity in the upper layer, but the lack of winds keeps the signal from propagating downward. The seasonal pycnocline traps the freshwater, and as austral fall progresses and winds increase, the fresh signal is mixed downward and saltier water from deeper depths are mixed upward. The saltiest the surface salinity is in the spring, before the shallow mixed layer of the summer season begins.

| | SAFDE | | cDrake | |
|---|---|---|---|---|
| | **min** | **max** | **min** | **max** |
| $\tau$ | -0.3 ms | 0.35 ms | -0.5 ms | 0.4 ms |
| T | -1.0°C | 0.7°C at the surface | -1°C | 1.2°C at the surface |
| | -0.1°C | 0.1 °C at 200 dbar | -0.1 °C | 0.1 °C at 140 dbar |
| S | -0.04 PSU | 0.08 PSU at the surface | -0.05 PSU | 0.02 PSU at the surface |
| | -0.01 PSU | 0.01 PSU at 200 dbar | -0.01 PSU | 0.01 PSU at 130 dbar |

Table 1.1: Seasonal cycle correction for cDrake (right column) and SAFDE, Subantarctic flux and dynamics experiment, *Watts et al.* [2001] (left column) for $\tau$ (top row), temperature (middle rows) and salinity (bottom rows).

Since the cDrake array covers a large geographical distance with the transport line, it is possible that the seasonal cycle varies with latitude. XCTDs cannot be deployed south of 61°S due to pollution regulations, so the database cannot assess any latitudinal dependence of the seasonal cycle. While the CTD database did not provide enough temporal coverage during the austral winter months to resolve the salinity cycle, it does resolve a similar temperature signal as the XCTDs and the CTD casts extended to the southern end of Drake Passage. The latitudinal dependence of the salinity cycle could

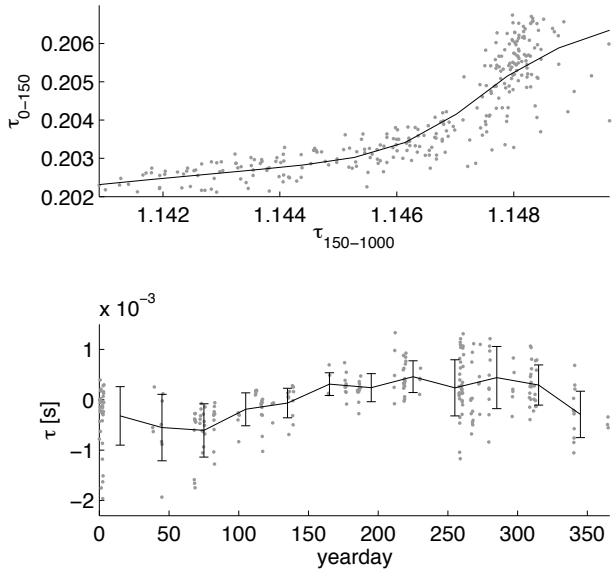


Figure 1.4: Upper panel: Seasonally varying upper-ocean $\tau_{0-150}$ from the XCTD data plotted versus deep-ocean $\tau_{150-2000}$. A spline (black line) is fit to the estimates (gray dots). Lower panel: The residual from the spline fit in the upper panel plotted as a function of generic year day (gray dots). A 90-day running mean applied to the residual (black line) is shown with standard deviation estimates for 30-day bins.

not be assessed with the available data sets.

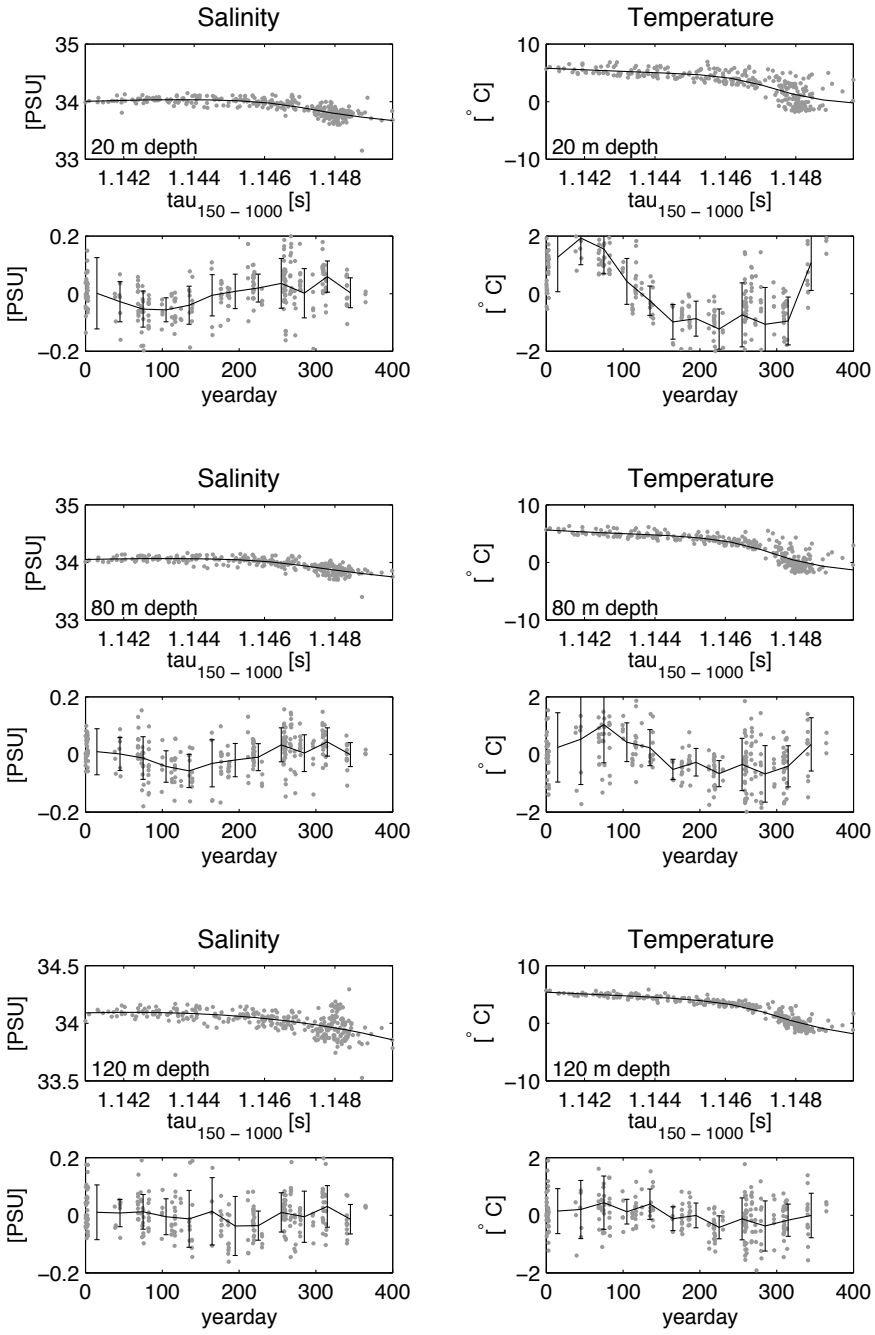


Figure 1.5: Seasonal cycle determined with XCTD data for salinity (left) and temperature (right). For three selected depths, two plots are shown. In the upper-panel pair salinity or temperature is plotted as a function of deep-ocean $\tau_{150-2000}$. Gray dots represent individual XCTD cast values and the black line is the spline fit to the data. In the lower panel of each pair, the gray dots show the residual between the data and fit from the upper panel, plotted as a function of generic yearday. The black line is a 90-day running average of the residual shown with standard deviation error bars calculated in 30-day bins.

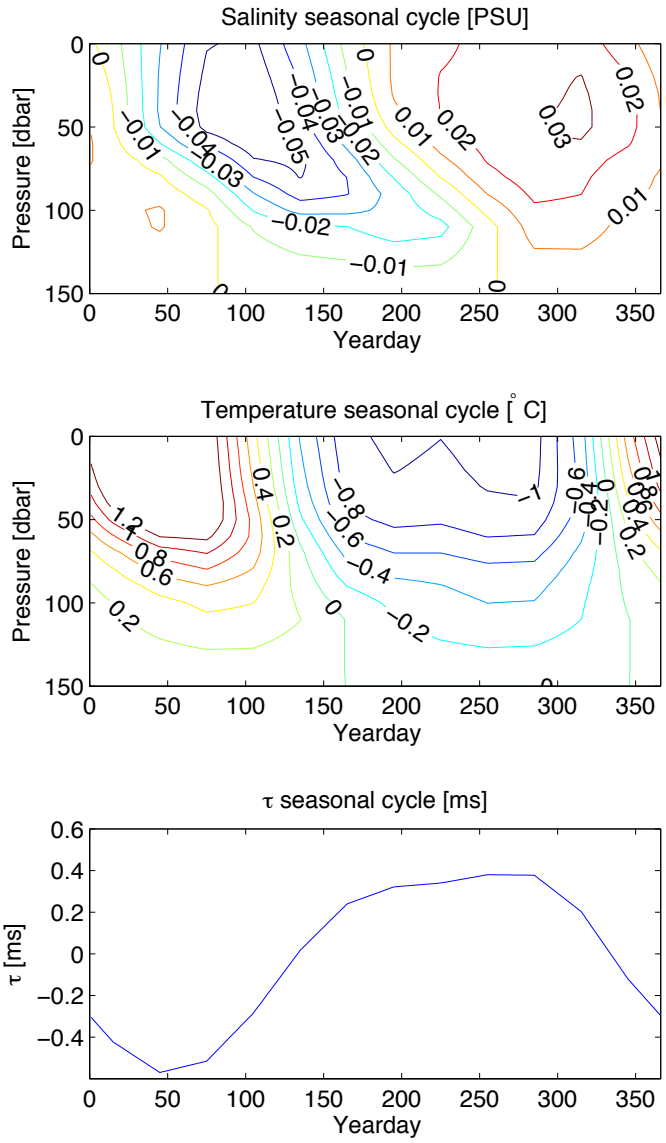


Figure 1.6: Salinity (top) and temperature (middle) seasonal cycles contoured for the upper 200 dbar as a function of generic yearday. $\tau_{0-150}$ (lower panel) plotted as a function of generic yearday.

### 1.2.3 GEM Construction

A Gravest Empirical Mode (GEM) is a look-up table between a hydrographic property such temperature, salinity, specific volume anomaly, or geopotential and an index, vertical acoustic round trip travel time ($\tau$). It is created with historical hydrographic data [*Meinen and Watts*, 2000]. The cDrake GEM for temperature and salinity are shown in figures 1.8 and 1.9. The GEM technique has been successfully utilized in the Southern Ocean [*Watts et al.*, 2001].

For the cDrake experiment, $\tau_{index}$ was round trip travel time integrated between the surface and 2000 dbar. In choosing the lower bound for this integral, there was a tradeoff between having enough casts to construct the GEM while still capturing the variability at greater depths. Depths deeper than 2000 dbar did not significantly improve the accuracy of the GEM and there were more than four hundred casts that reach at least 2000 m depth. For example, at 500 dbar the root mean square (RMS) of temperature (salinity) was 0.23°C (0.05 PSU) with 409 casts for $\tau_{2000}$ and 0.23°C (0.04 PSU) with 290 casts for $\tau_{3000}$. Table 1.2 shows values at other depths and for GEMS made with either different indices or including the seasonal cycle in the upper 150 m.

Historical hydrography were gathered to construct the GEM for the time period 1970 to 2009 (figure 1.7). The latitudinal extent of the region selected for the GEM was dictated by land masses, while the longitudinal extent was chosen based on the range of $\tau$ values for the casts found in those regions. Further extension to the west included few additional casts and showed no improvement to the GEM, and expanding to the east included waters that were not representative of those in Drake Passage. The final box chosen was 12° in longitude, which is similar to the 10° bin used by *Sun and Watts* [2001]. Most CTD casts occurred during the austral summer months. Data were gathered from many sources, including the Southern Ocean database, Argo float profiles, and various other modern Drake Passage field programs. Only casts with good vertical resolution were included and all casts were quality controlled. Casts reaching to at least 2000 m depth were used in the construction of the GEM (figure 1.7).

The variability in the GEM decreases with depth in both temperature and salinity. In the temperature GEM (figure 1.8), the RMS was highest in the surface layers in the upper 200 m. Since the seasonal cycle has been removed, the upper-ocean variability must be due to other processes. Two major high RMS features extended down to 200 dbar. For low $\tau$, this high variability associates with Subantarctic Mode Water. For high $\tau$, the variability could be due to Upper Circumpolar Deep Water, Lower Circumpolar Deep Water, and North Atlantic Deep Water variability [*Speer et al.*, 2000]. The salinity GEM variability is highest in the upper 1500 m. The increased RMS values are for salinities less than 34.6 PSU for $\tau$ shorter than 2.687 s. For the higher $\tau$ values, the increased variability could be due to deep water formation and ice formation and melt along the Antarctic coast.

| | $\tau_{0\text{-}2000}$ with seasonal cycle | $\tau_{0\text{-}2000}$ removing seasonal cycle | $\tau_{0\text{-}3000}$ removing seasonal cycle |
|---|---|---|---|
| # CTD casts | 409 | 409 | 290 |
| RMS at 50 dbar of T | 0.986 | 0.625 | 0.621 |
| 50 dbar of S | 0.104 | 0.104 | 0.062 |
| 500 dbar of T | 0.234 | 0.227 | 0.234 |
| 500 dbar of S | 0.050 | 0.048 | 0.042 |
| 1000 dbar of T | 0.103 | 0.091 | 0.076 |
| 1000 dbar of S | 0.031 | 0.030 | 0.026 |
| 1500 dbar of T | 0.083 | 0.073 | 0.056 |
| 1500 dbar of S | 0.019 | 0.019 | 0.016 |
| 2000 dbar of T | 0.089 | 0.082 | 0.060 |
| 2000 dbar of S | 0.013 | 0.013 | 0.011 |
| 3500 dbar of T | 0.106 | 0.103 | 0.095 |
| 3500 dbar of S | 0.005 | 0.005 | 0.005 |

Table 1.2: Comparison between three GEM constructions (columns two through four). For each GEM, the number of CTD casts are noted in the first row and subsequent rows provide the RMS of the spline fit for temperature and salinity at selected depths.

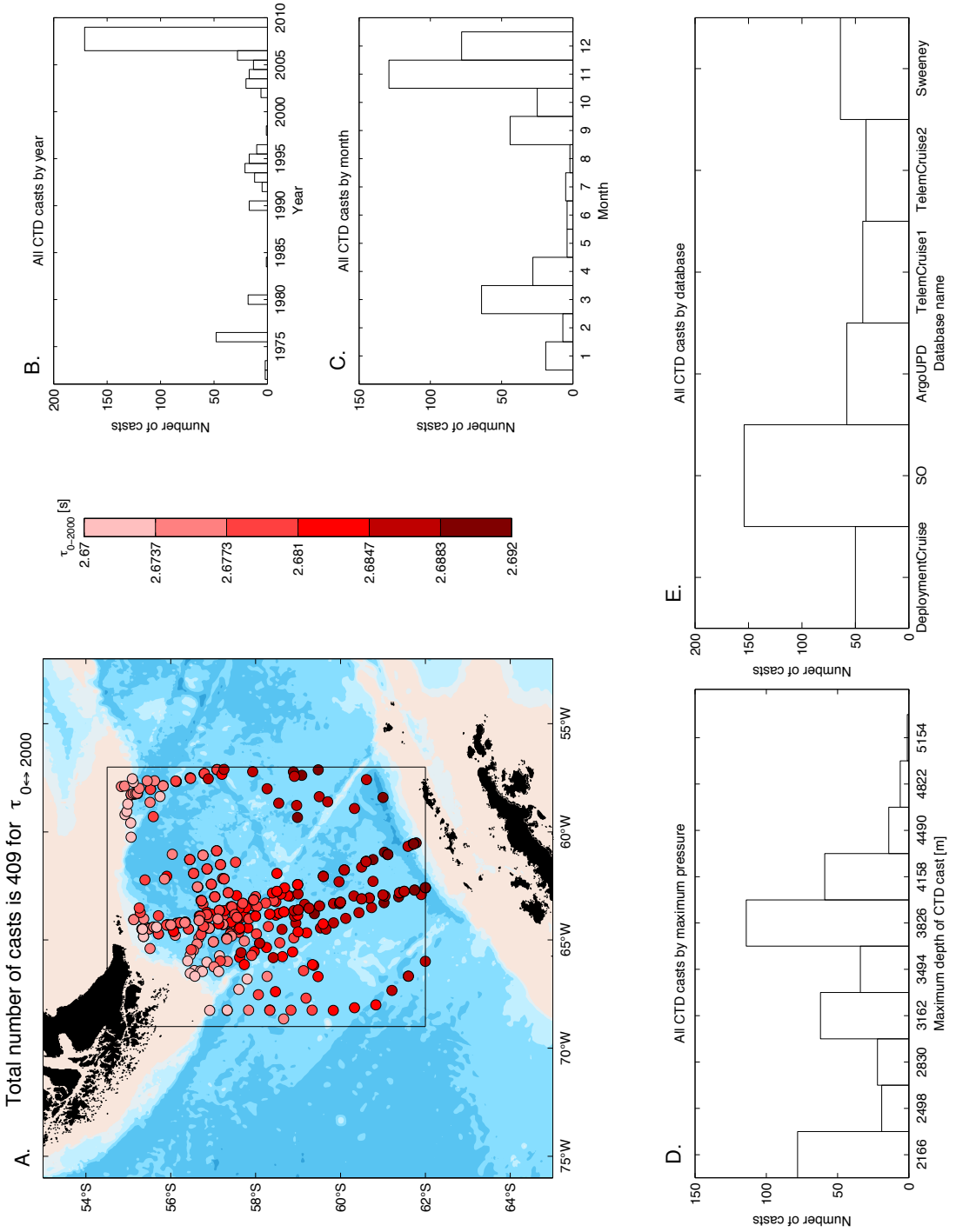


Figure 1.7: a) Location of the 409 CTD casts used to construct the final GEM. Each cast is color-coded by $\tau_{0-2000}$ value and the colorbar is provided to the right of the map. Distribution of casts by year (b), month (c), maximum pressure (d), and data source (e).

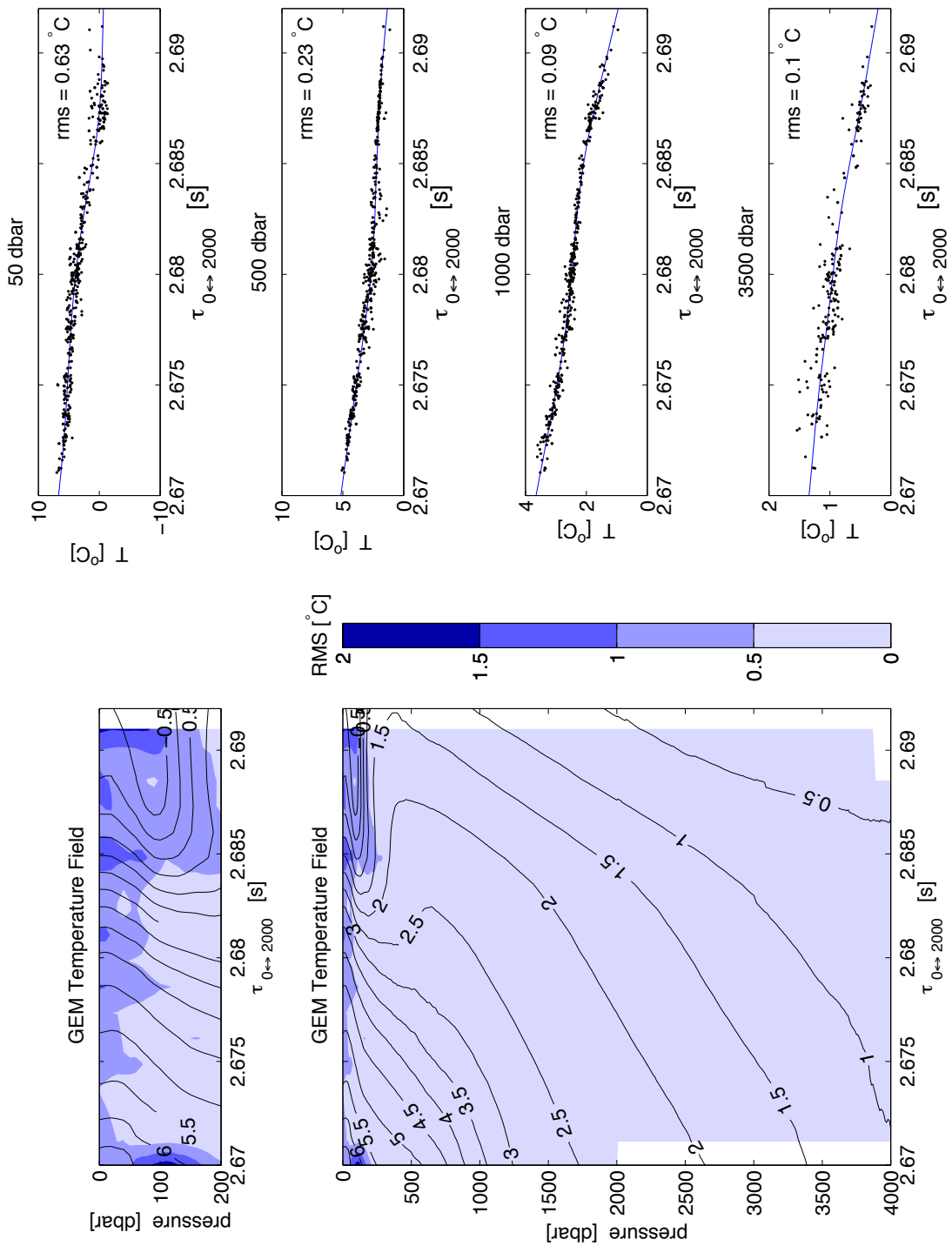


Figure 1.8: Temperature GEM for Drake Passage. Left panels: Temperature contoured as a function of pressure (black lines) and $\tau_{0-2000}$. Contour interval is 0.5°C. The upper left panel extends from 0 to 200 dbar to emphasize the upper-ocean structure. Right panels show temperature at selected depths plotted as a function of $\tau_{0-2000}$ (black dots) with the superimposed spline fit (blue line). The residual of the fit is denoted in the upper right corner of each plot and color-shaded in the left panels. A colorbar to the right of left panels provides the RMS color scale.

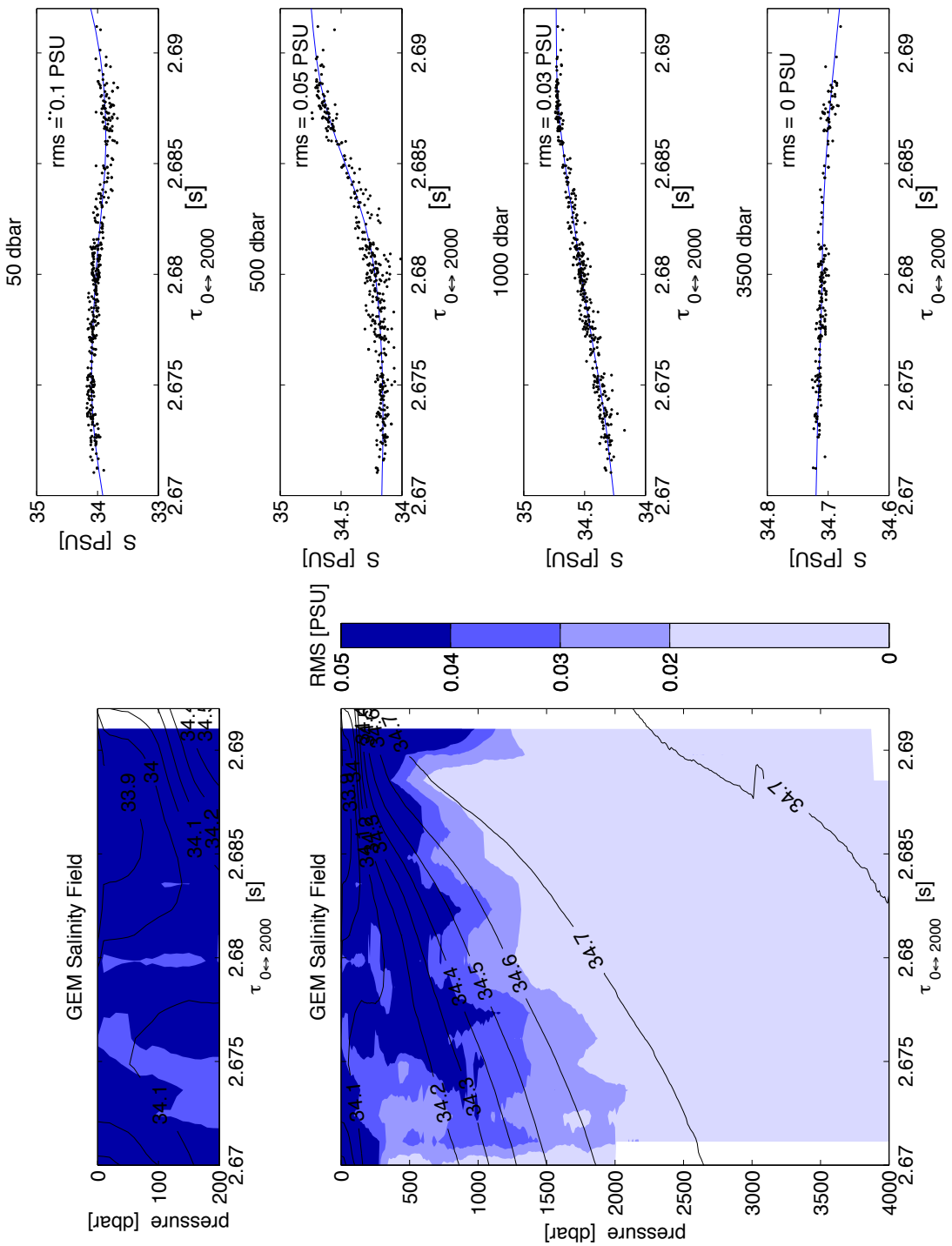


Figure 1.9: Salinity GEM for Drake Passage. Left panels: Salinity contoured as a function of pressure (black lines) and $\tau_{0-2000}$. Contour interval is 0.1 PSU. The upper left panel extends from 0 to 200 dbar to emphasize the upper-ocean structure. Right panels show salinity at selected depths plotted as a function of $\tau_{0-2000}$ (black dots) with the superimposed spline fit (blue line). The residual of the fit is denoted in the upper right corner of each plot and color-shaded in the left panels. A colorbar to the right of left panels provides the RMS color scale.

At site C17 at the southern tip of the transport line along the Antarctic continental slope, the shallow depth of 1280 m and long $\tau$ values posed a challenge. Despite CTD casts near the site, after recovering the first year of data it was discovered that the GEM with 2000 dbar reference level did not have long enough travel times to accommodate all of the signals at C17. It proved impossible to find casts with long enough travel times that reached 2000 dbar, so a new GEM was created for use at only site C17. The same method was employed, but by raising the reference level to 1000 dbar and expanding the geographical area to include hydrographic data to the east and along the coast, more appropriate $\tau$ values were found (figure 1.10). It appears that the cold water advects from east to west near site C17. During the second telemetry cruise, fourteen CTDs were taken between 61.4°W and 59.4°W and 61.75°S and 62.25°S. This increased the number of casts with long $\tau_{0-1000}$ values in the C17 GEM. The accuracy of this new shallower GEM ($\tau_{0-1000}$, figures 1.11 and 1.12) is comparable to that of the GEM ($\tau_{0-2000}$) used for the rest of the array. For $\tau_{0-1000}$, the RMS of temperature (salinity) at 500 dbar was 0.198°C (0.047 PSU), compared to $\tau_{0-2000}$ with 0.227°C (0.048 PSU).

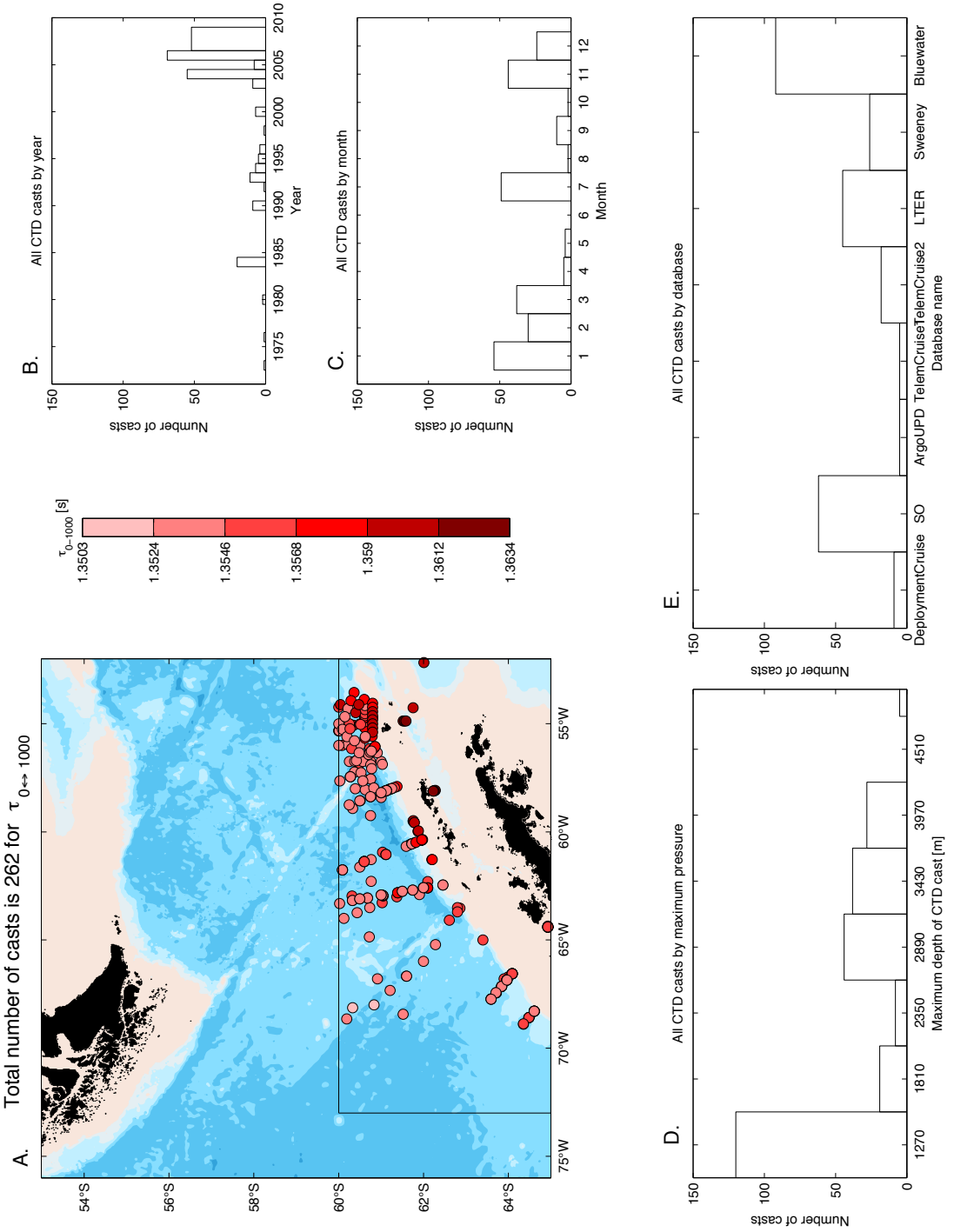


Figure 1.10: a) Location of the 262 CTD casts used to construct the final $\tau_{0-1000}$ C17 GEM. Each cast is color-coded by $\tau_{0-1000}$ value and the colorbar is provided to the right of the map. Distribution of casts by year (b), month (c), maximum pressure (d), and data source (e).

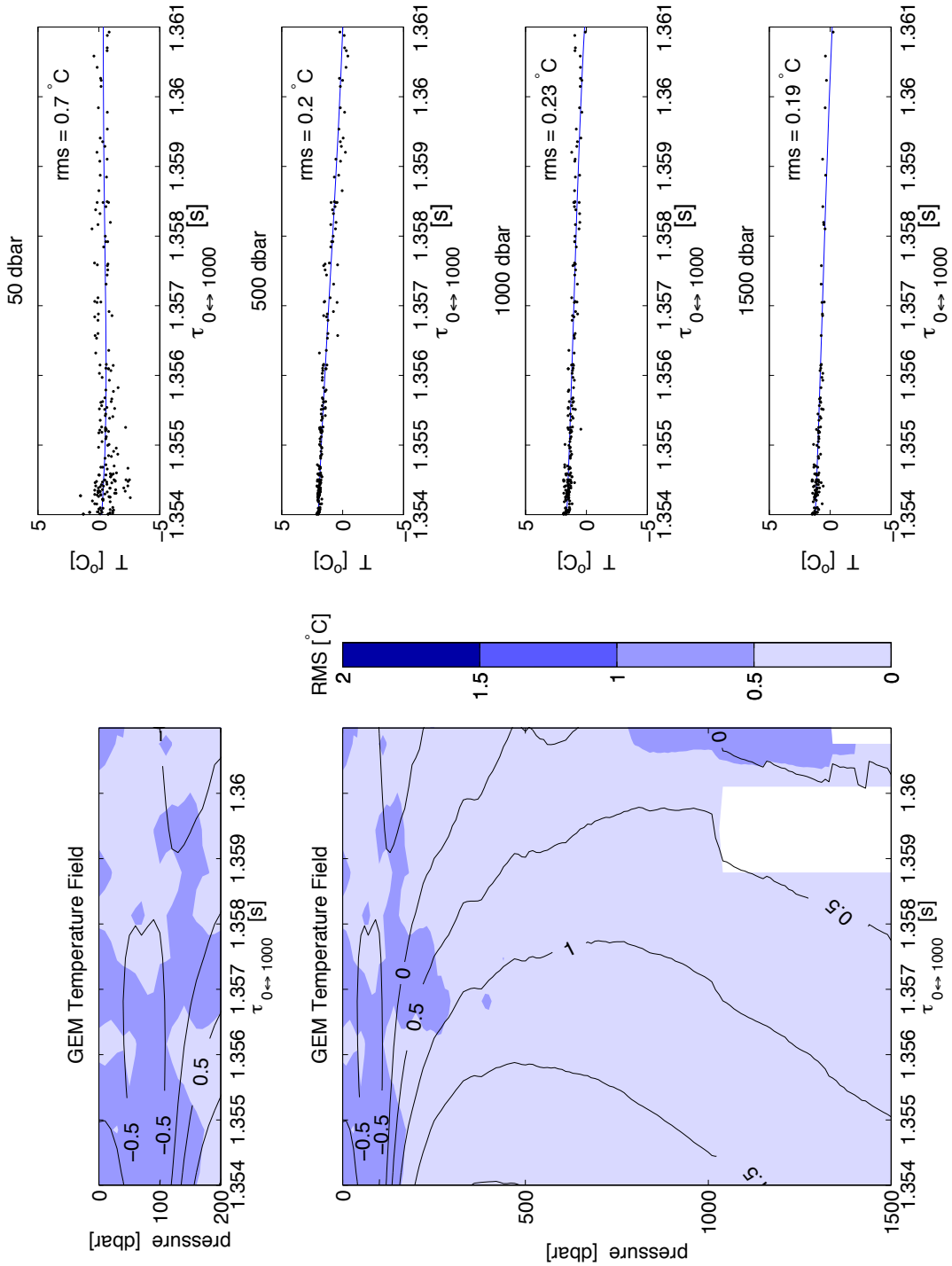


Figure 1.11: Temperature GEM for site C17. Left panels: Temperature contoured as a function of pressure (black lines) and $\tau_{0-1000}$. Contour interval is 0.5°C. The upper left panel extends from 0 to 200 dbar to emphasize the upper-ocean structure. Right panels show temperature at selected depths plotted as a function of $\tau_{0-1000}$ (black dots) with the superimposed spline fit (blue line). The residual of the fit is denoted in the upper right corner of each plot and color-shaded in the left panels. A colorbar to the right of left panels provides the RMS color scale.

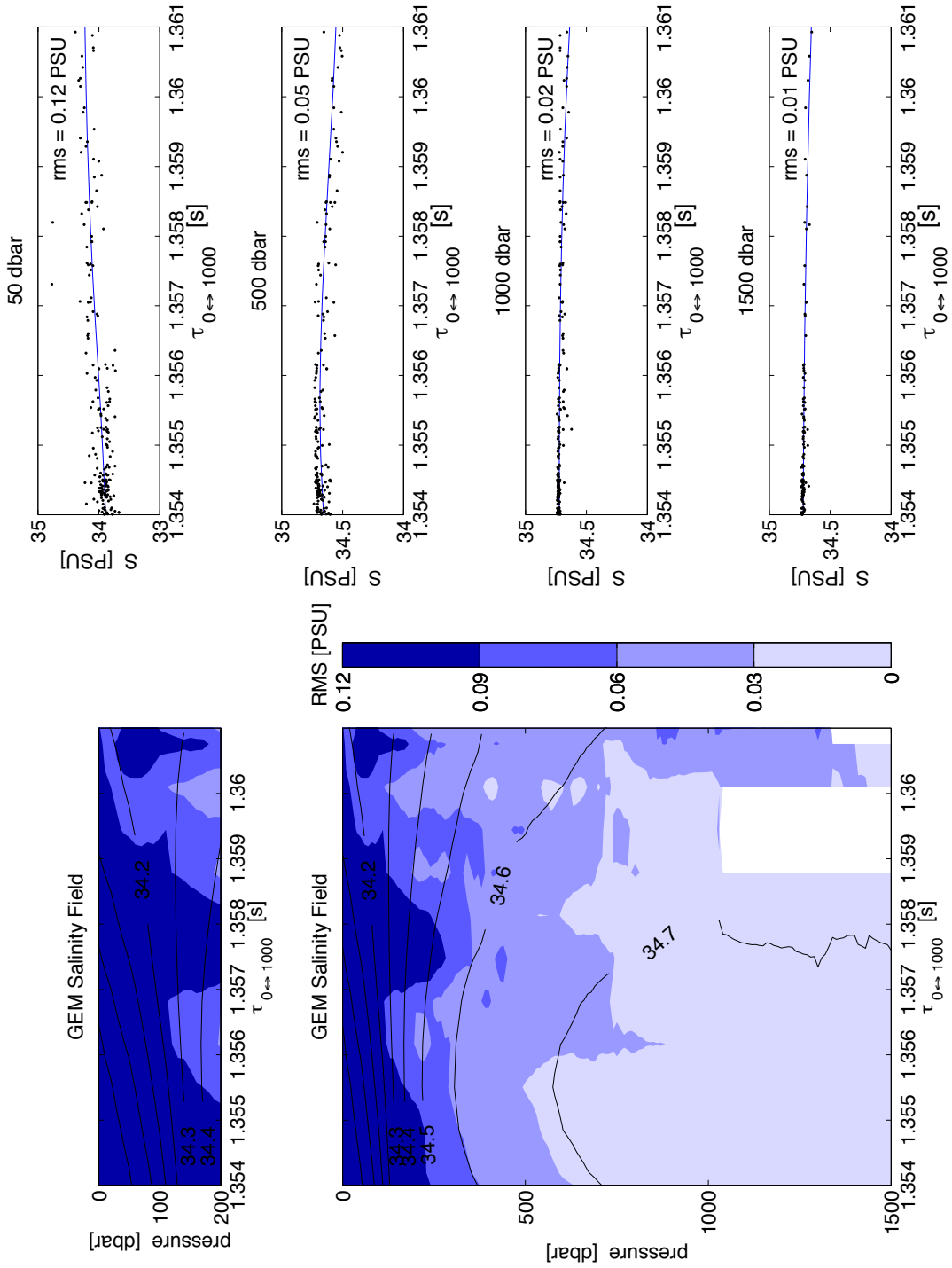


Figure 1.12: Salinity GEM for site C17. Left panels: Salinity contoured as a function of pressure (black lines) and $\tau_{0-1000}$. Contour interval is 0.1 PSU. The upper left panel extends from 0 to 200 dbar to emphasize the upper-ocean structure. Right panels show salinity at selected depths plotted as a function of $\tau_{0-1000}$ (black dots) with the superimposed spline fit (blue line). The residual of the fit is denoted in the upper right corner of each plot and color-shaded in the left panels. A colorbar to the right of left panels provides the RMS color scale.

### 1.2.4 CPIES-Data Processing

The CPIES measure the vertical round-trip travel time from the seafloor to the surface and back, as well as recording pressure at the seafloor and current speed and direction 50 m above the seafloor. The focus in this work was on the pressure and travel-time measurements. The current speed and direction were used only in aiding the removal of pressure drifts from the bottom-pressure sensors. Most of the analysis was performed on a 2-year record of daily averages that were acoustically telemetered from the instruments on the sea floor to a ship on the surface. Due to technical issues, 18 instruments were recovered. Sites C09, D01 and E01 in 2008 and sites A01 and B03 in 2009 were recovered because shipboard diagnostics suggested noisy $\tau$ data. These instruments provided hourly measurements. Once recovered, more sophisticated processing of hourly records can often improve the quality of the $\tau$ data. Spectral analysis of telemetered records at sites B02 and E02 revealed that the $\tau$ values were noisy, and will therefore have higher variance at high frequencies. The processing of the hourly and telemetered records is explained in the following sections.

The inverted echo sounder in the CPIES emits a 12.0 kHz pulse 24 times per hour and measures the amount of time it takes for the ping to reflect off the sea surface and return to the detector. These measurements were stored in the instrument, and were available upon recovery. The 24 pings were processed with a two-stage windowing and median filtering to reduce scatter associated with sea surface roughness, yielding an hourly measurement. The bottom pressure gauge measured every half hour and were averaged to create an hourly estimate. In an effort to reduce pressure drift, each sensor was pre-stressed. Despite this, there was still some residual drift in each pressure record. A linear plus an exponential curve was removed from the pressure measurements at each site as in *Donohue et al.* [2010]. Response analysis removed the semidiurnal and diurnal tides [*Munk and Cartwright*, 1966]. The largest constituent was the semidurnal M2 tide with an amplitude of 37-47 cm. The next largest were K1 and O2 (15-23cm), S2 (8-15 cm), and N2 (6-11 cm). P1, Q1 and K2 were all <6 cm each. The lunar monthly and

fortnightly tides were removed using the Oregon State University tidal model [*OSU*, 2009]. The fortnightly tide had an amplitude less than 3 cm and the monthly less than 1 cm.

Prior to recovery, annual telemetry cruises collected daily-average values of $\tau$ and pressure. Thus the telemetered data required different but analogous processing from the above hourly data. The CPIES instruments internally processes the $\tau$ measurements by windowing and median filtering, and then computes a daily average. The pressure daily-average values were internally computed using a Godin filter to remove the diurnal and semidiurnal tides. The data in this study were collected on two telemetry cruises in 2008 and 2009. Post-processing further low-pass filtered with a 3-day cutoff and removed the lunar and fortnightly tides using the Oregon State University tidal model [*OSU*, 2009].

The CPIES-measured $\tau$ were converted to $\tau_{index}$ as outlined in *Donohue et al.* [2010]. First, the contribution to $\tau$ from the mass-loading constituent was removed to make $\tau$ purely steric. The bottom pressure record was converted to an equivalent acoustic path length and then subtracted from $\tau_{measured}$. Next, the latitudinal and depth dependence of gravity was removed as in *Donohue et al.* [2010] using the equation:

$$\tau_{dynamic} = \tau_{measured} \left( \frac{g(\lambda, 0)}{9.8 \left(1 - \frac{P}{1.017R}\right)} \right) \tag{1.2}$$

where g is gravity as a function of latitude ($\lambda$) at the sea surface, 9.8 is gravity in $\mathrm{ms}^{-2}$, $P$ is the depth of the instrument in dbar, and $R$ is the radius of the earth (6371 km). The seasonal signal (figure 1.6) was removed from dynamic $\tau$. The final step was a conversion from this $\tau_{dynamic}$, which was a full water column round-trip travel time, to the $\tau_{index}$ of the GEM look-up table. This was accomplished by fitting a polynomial to the $\tau_{dynamic}$ versus $\tau_{0-2000}$ relationship. The final $\tau_{index}$ time series were combined with the GEM look-up tables to produce daily temperature profiles, salinity profiles, or geopotential at each site.

There are six or seven independent sources of error for hourly or daily measurements, respectively (table 1.3). Error estimates for $\tau_{index}$ closely follow *Donohue et al.* [2010]. The return acoustic signal contains scatter due to sea surface roughness. This error was

determined by calculating the standard deviation of the scatter of all individual pings that are the basis of each measurement and dividing by the square root of the number of measurements. This yielded a 0.34 ms error for the hourly estimate and a 0.07 ms for the daily estimate (Row 1 in table 1.3). The conversion from $\tau_{measured}$ to $\tau_{index}$ has error from several sources. First, the measurement must be a steric signal free of any influence from barotropic processes. When creating a purely steric $\tau$, the bottom pressure record was converted to an equivalent acoustic path length and then subtracted from $\tau_{measured}$. Uncertainty in the pressure drift contributed the largest source of error to this adjustment of $\tau$ and was estimated as 0.02 ms (Row 2 in table 1.3). The accuracy of the conversion from $\tau_{measured}$ to $\tau_{dynamic}$ is six parts per million, so given an average depth of 4000 m, the error in the cDrake region was 0.03 ms. Third, measured $\tau$ has not been corrected for the pathlength due to the inverted-barometer response of the sea surface. RMS from the European Center for Medium-Range Weather Forecasts (ECMWF) operational archive atmospheric pressure fields determined the RMS variation of atmospheric pressure in Drake Passage to be 0.2 dbar, with corresponding path-length error in $\tau$ of 0.27 ms. Fourth, daily records have error associated with the acoustic telemetry. Comparison between the telemetered records received on the ship with the files stored within recovered instruments determined the 0.27 ms of telemetry error. At the conclusion of the cDrake experiment, the recovered records instrument data sets will eliminate this error and improve the accuracy of the CPIES measurements. Fifth, the conversion from $\tau_{dynamic}$ to $\tau_{0-2000}$ (the index of the GEM look-up) was the single largest source of error. It was estimated by the scatter in plotting $\tau_{0-2000}$ versus $\tau_{0-3500}$ for deep CTD hydrocasts and is 0.46 ms. Finally, upper-ocean variability contributes an error. This is due to seasonal and interannual variability in wind-induced mixing, atmospheric heating, and changes in freshwater inputs from precipitation, ice formation, and ice melt. The seasonal cycle was removed to help reduce this error, but the remaining scatter introduced to $\tau_{0-2000}$ from the upper $\tau_{0-200}$ was one of the largest errors in the steric SSHA (line 6). This was reduced from 0.58 ms to 0.44 ms by removing the seasonal cycle. The total error in

$\tau_{0-2000}$ was 0.77 ms (0.70 ms) for the hourly (daily) estimates and was determined by taking the square root of the sum of the squares of the independent errors.

| | **$\tau$ Errors** | | |
|---|---|---|---|
| | | Hourly | Daily |
| 1 | Scatter in $\tau_{measured}$ /($N^{1/2}$) [ms] | 0.34 | 0.07 |
| 2 | Steric correction [ms] | 0.02 | 0.02 |
| 3 | $\tau_{dynamic}$ [ms] | 0.03 | 0.03 |
| 4 | IB pathlength error [ms] | 0.27 | 0.27 |
| 5 | Telemetry error [ms] | | 0.27 |
| 6 | Upper ocean variability [ms] | 0.44 | 0.44 |
| 7 | $\tau_{dyn}$ to $\tau_{index}$ [ms] | 0.46 | 0.46 |
| 8 | **Total error in $\tau_{index}$ [ms]** | **0.77** | **0.75** |

Table 1.3: CPIES $\tau_{index}$ errors.

### 1.2.5 Computation of Sea Surface Height Anomaly from CPIES

The definition of sea surface height can be derived starting from the integral of the hydrostatic equation as in *Baker-Yeboah et al.* [2009],

$$\int_{-H}^{\eta'} dz = -\int_{p_{bot}}^{p_a} \frac{1}{\rho g} dp, \tag{1.3}$$

where $\eta = \overline{\eta} + \eta'$ is total SSH, $\overline{\eta}$ is mean SSH over the record length, $\eta'$ is SSH anomaly, $H$ is the ocean depth, $\rho$ is the density of seawater, $g$ is gravity, $p_a$ is the surface atmospheric pressure, and $p_{bot}$ is seafloor bottom pressure. Evaluating the integral on the left hand side and redefining the integral on the right hand side of equation 1.3 yields

$$\eta' + H = \int_{\overline{P}_a}^{p_{bot}} \frac{1}{\rho g} dp + \frac{p'_a}{\rho_s g}, \tag{1.4}$$

where $p'_a = p_a - \overline{P}_a$ is the variation in surface atmospheric pressure relative to a mean $\overline{P}_a$ and $g$ is the local gravitational acceleration. After further manipulation,

$$\eta' - \eta_{IB} + (H - H_{so}) = \frac{\phi_{\overline{P}}}{g} + \frac{p_{bot} - \overline{P}}{\rho_b g} \tag{1.5}$$

where $\eta'$ is the time-varying component of SSH, $\eta_{IB}$ is the inverted barometer response, $H$ is the mean ocean depth at one geographic location, $H_{so}$ is the mean standard ocean depth, $\phi_{\overline{P}}$ is the geopotential anomaly, $\overline{P}$ is the average bottom pressure, and $\rho_b$ is bottom density. $\eta_{IB}$ represents the sea level response that the ocean would have to atmospheric pressure if the bottom pressure were unaffected. The travel-time measurements have not been corrected for the pathlength change due to the change in atmospheric pressure. On the right hand side of equation 1.5, the first term represents the steric component and the second term represents the mass-loading component of SSH.

In this work, sea surface height anomaly (SSHA) will be utilized. The steric component of SSHA is given by the first term on the right hand side of equation 1.5 with mean removed,

$$\eta'_s = \frac{\phi'_{\overline{P}}}{g}. \tag{1.6}$$

The GEM was used to convert from $\tau_{index}$ to temperature and salinity profiles, which in turn were used to compute $\phi'_{\overline{P}}$ and steric SSHA. The second term on the right hand side

in equation 1.5, substituting bottom pressure anomaly for total bottom pressure,

$$\eta'_m = \frac{p'_{bot}}{\rho_b g}, \tag{1.7}$$

is the mass-loading constituent of SSH. The term was calculated using the time series of bottom pressure provided by the CPIES. In the above equations, the SSH and its components were computed relative to the instrument's depth. Referencing SSHA to the seafloor resulted in two modes that can be identified with physical modes, a baroclinic mode which contained the shear/steric signal and a barotropic/mass-loading mode which was depth independent.

Note that for the analysis of the SSHA data calculated from the CPIES, the seasonal signal has also been removed from the measurements. Altimetric products do not remove the seasonal cycle, so for comparisons between the cDrake and AVISO data, the seasonal signal has been added back in to the CPIES data.

In addition to the error in the $\tau_{2000}$ values as outlined in the previous section, there are more errors associated with both the steric and mass-loading constituents of SSHA. As an upper bound on the error for the cDrake region, individual contributions to the total error in steric $\tau$ for hourly (daily) measurements was 7.29 cm (7.16 cm) as shown in table 1.4. Because $\tau$ was used as proxy to determine temperature and salinity to compute geopotential ($\phi$), there was an error associated with the look-up tables. The error in the geopotential itself was calculated by taking the RMS difference between $\phi$ computed from CTD casts and the value of $\phi$ from the GEM given the CTD casts $\tau_{0-2000}$ value. For cDrake, this error expressed as $\delta\phi$ was 0.49 $\mathrm{m^2 s^{-2}}$. The relationship between $\phi$ and $\tau_{0-2000}$ was linear with a slope $\frac{\partial\phi}{\partial\tau}$ of -0.68. The total error associated with the look-up between travel time and geopotential is

$$\epsilon_\phi = \sqrt{\left(\left|\frac{\partial\phi}{\partial\tau}\right|\delta\tau\right)^2 + (\delta\phi)^2}. \tag{1.8}$$

Dividing $\epsilon_\phi$ by gravity yields the total error in steric SSHA, which for the hourly measurements is 7.29 cm and for daily measurements is 7.16 cm. Error in barotropic SSHA derives from measurement error and uncertainty in the determination of the pressure

drift. Based upon values determined in the Kuroshio Extension System Study [*Donohue et al.*, 2010], an estimate of 0.72 cm is used here.

The values for total SSHA error were slightly higher than those from *Baker-Yeboah et al.* [2009] in the Agulhas Retroflection region, which had an error of 5.6 cm for total SSHA. Unlike *Baker-Yeboah et al.* [2009], this study quantified the upper-ocean variability in $\tau$ and partially corrected for a seasonal signal. No upper-ocean variability was accounted for in the Agulhas Retroflection study. In addition, the daily values for the cDrake experiment included a telemetry error. The combination of these errors accounts for the discrepancies in error values.

| | **Steric SSHA Errors** | | |
|---|---|---|---|
| | | Hourly | Daily |
| 1 | Slope of $\phi_{3500}$ versus $\tau_{2000}$ [$m^2\ s^{-2}\ ms^{-1}$] | -0.68 | -0.68 |
| 2 | Error in $\phi$ lookup [$m^2\ s^{-2}$] | 0.49 | 0.49 |
| 3 | Total error in $\phi$ [$m^2\ s^{-2}$] | 0.71 | 0.70 |
| 4 | **Total error in Steric SSHA [cm]** | **7.29** | **7.17** |

| | **Mass-loading SSHA Error** | | |
|---|---|---|---|
| | | Hourly | Daily |
| 5 | **Total error in mass-loading SSHA from paired site comparisons [cm]** | **0.72** | **0.72** |

Table 1.4: CPIES-derived sea surface height anomaly errors.

Error was also estimated for the cDrake CPIES steric SSHA by finding the noise floor from spectral analysis. Due to the large changes in total variance across the passage, a separate noise floor was found from the sites north and south of 58.5°S. Figure 1.13 shows the difference in noise floor between the two regions. The northern sites had a variance floor of 0.001 $m^2$, whereas the southern sites had only 0.0003 $m^2$. The error in steric SSHA was calculated by

$$\epsilon = \sqrt{V \ln\left(\frac{0.5}{0.0078}\right)} \tag{1.9}$$

where $\epsilon$ is the error, $V$ is the noise floor, and 0.5/0.0078 is the ratio of the highest to

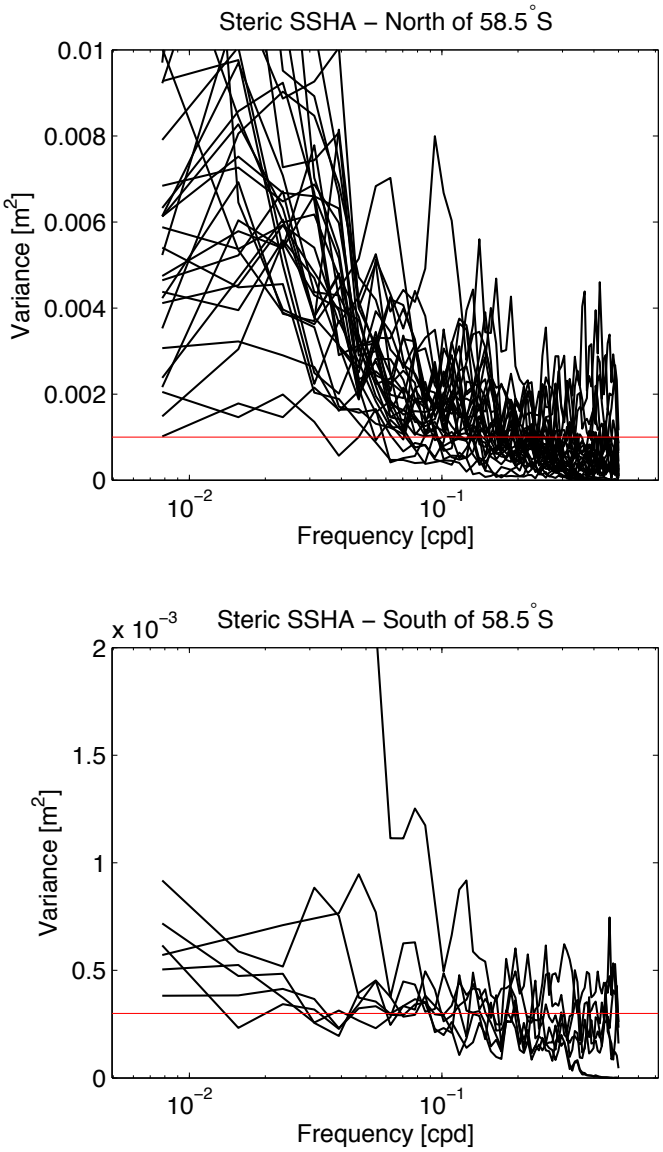


Figure 1.13: Steric SSHA variance as a function of frequency for sites north (south) of 58.5°S in black in the upper (lower) panel and the noise floor for each region in red .

lowest frequency for the dataset. The northern sites had an error of 6.5 cm, which is close to the estimate from the tabulated errors in table 1.4. The southern sites, however, had an error of only 3.5 cm from the spectral estimate, which is much lower than the values in the northern sites.

### 1.2.6 Satellite Altimetry

Satellite altimeter products are produced by SSALTO/DUACS and distributed by AVISO, with support from CNES (http://www.aviso.oceanobs.com/duacs/). Two satellite altimeters occupy Drake Passage for the length of the cDrake deployment. The first is the Jason-2 satellite whose groundtracks have a spacing of 315 km at the equator and a 10-day repeat. The ERS satellite has much higher spatial resolution, more than triple that of the Jason satellites with 90 km resolution at the equator. The ERS repeat interval is longer than Jason occurring once every 35 days. These two satellites are combined into the delayed-time, merged, reference, gridded sea level anomaly maps with temporal resolution of 7 days mapped to a 1/3° grid. Satellite tracks and their relationship to the cDrake array are shown in Figure 1.1. All except 6 sites fell along an ERS track and only 7 sites fell on a Jason track.

The Aviso along-track products from the Jason and ERS satellites had errors of 3.4 cm [*Aviso*, 2008]. The merged product contains the same error in the individual measurements, as well as the error from the mapping process. Aviso provides weekly maps of the mapping error with the SSHA measurements [*Aviso*, 2010]. The time series in figure 1.14 show the range of the mapping error for sites C04, D02, and C14. Errors were higher when there was a strong SSHA event, such as a frontal meander or eddy. The range at the northern transport line and LDA sites was 3 cm and the southern transport sites peaked at 2 cm. Mapping errors combined with the along-track measurement error yielded total errors ranging from 3.4 cm to 4.5 cm. The time series of SSHA for sites C04, D02, and C14 are shown in figure 1.15 with total error bars.

Due to the low temporal resolution of the altimeters, any signals with a frequency under 1/20 cpd will not be resolved by the Jason-1 or Jason-2 altimeters, and signal frequencies under 1/70 cpd will not be resolved by ERS. The energy present in the ocean at higher frequencies than resolved by the altimeters can be aliased. In order to partially compensate for the atmospherically-driven component of this, Aviso applies what they call a dynamic atmospheric correction (DAC). Dynamic atmospheric

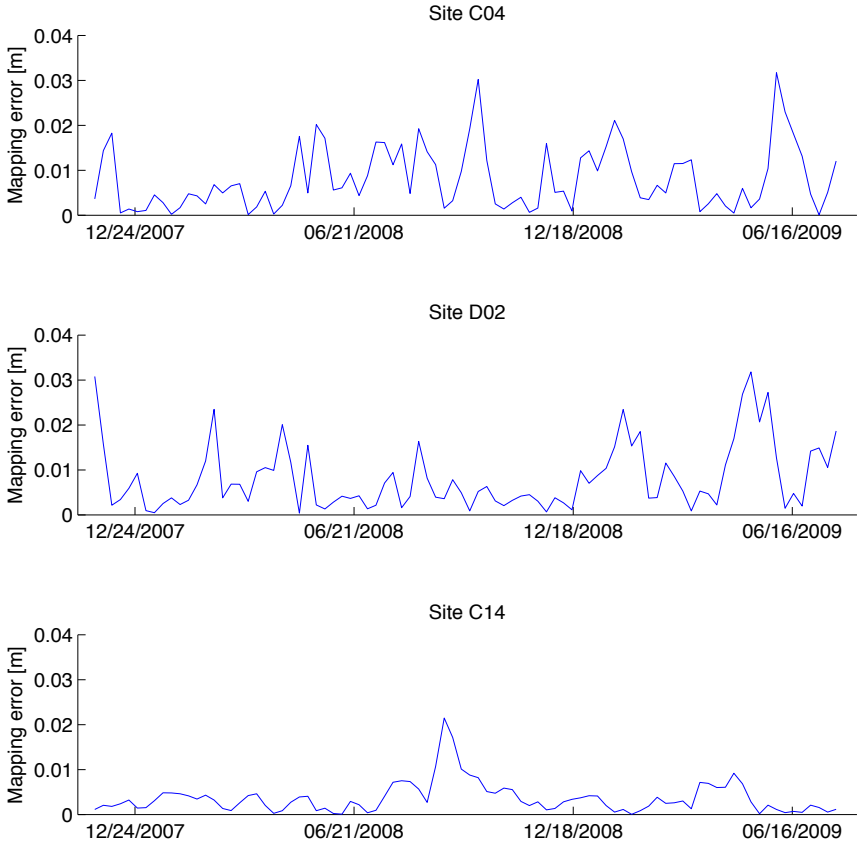


Figure 1.14: Aviso mapping error for the merged SSHA product as a function of time for 3 cDrake sites.

corrections are produced by CLS Space Oceanography Division using the a barotropic tidal mode, Mog2D model from Legos and distributed by Aviso, with support from Cnes (http://www.aviso.oceanobs.com/). The DAC consists of an inverted barometer (IB) correction and output from a wind and atmospherically forced barotropic model (Mog2D-G) on a 1/4° resolution global grid. The IB correction assumes a static response of the ocean to atmospheric pressure forcing and neglects the wind response. AVISO determines the ocean sea-level response to changes in atmospheric pressure using 6-hour 1/4 degree horizontal resolution European Center for Medium-Range Weather Forecasts (ECMWF) surface pressures [*Carrere and Lyard*, 2003]. The IB correction range is about 40 cm in Drake Passage. Mog2D-G is a high-resolution barotropic model with a finite element space discretization with resolution ranging from 400 km in the deep

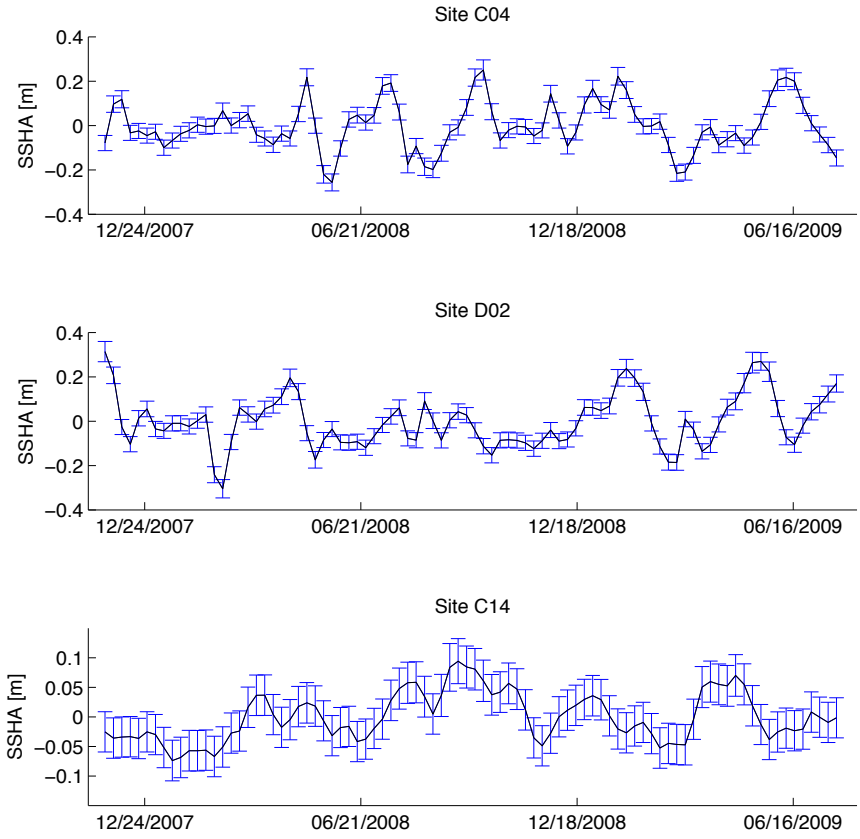


Figure 1.15: Aviso merged product SSHA time series for 3 cDrake sites, error bars are total measurement error.

ocean to 20 km in shallow coastal areas and is forced with 6-hour ECMWF wind and pressure. The high-frequency (HF) correction consists of the model output restricted to signals with frequencies greater than 1/20 cpd [*Carrere and Lyard*, 2003; *Volkov et al.*, 2007]. The DAC is applied to both the Jason and ERS satellites and is provided in the geophysical data records. This study utilized the Jason-2 along-track geophysical data records, which provide one value of the HF and IB every 10 days at the location and time of each Jason-2 measurement. (Note that the high-frequency correction is for signals greater then 1/20 cpd, even for the ERS satellite with a Nyquist frequency of 1/70 cpd. Aliasing of the energy between 1/20 cpd and 1/70 cpd is still possible).

## 1.3 Constituents of Sea Surface Height Anomaly

The character of sea surface height anomaly (SSHA) varied across Drake Passage in large part due to the meandering of the jets of the ACC. For example, consider a record in northern Drake Passage, at site C04. There variance was high and the steric signal dominates the total SSHA values for most of the record. The time series of SSHA showed that the range was almost a meter (figure 1.16, upper panel). Large shifts were attributed to the meandering Subantarctic Front (SAF). One of the most pronounced, low-frequency changes occurred in July and August 2008 when a high is followed by a low. To show how these events were due to SAF meanders and place them in a larger spatial context, the top row of figure 1.17 shows SSH maps for several days during major events and reveals that the SAF moved from south to north over the site over the course of two weeks.

In the local dynamics array, variance was also high, and large changes were due not only to SAF meanders but also PF meanders and eddies. D02 (middle panel of figure 1.16) exhibited SSHA variability that was of larger magnitude (1.2 m range) than observed at C04. At this site, both SAF and PF meanders and rings occurred, creating the larger range in SSH in the time series. There was a brief but strong low event in February 2008 which is shown in the progression of SSH maps in the middle row of figure 1.17 caused by a PF meander and eddy pinch-off. At the other extreme, a warm and high SSHA, SAF ring passed over the site in January 2009 while interacting with the SAF to the north and the PF to the south. As at C04, D02 was also dominated by the steric signal associated with the strong lateral gradient in SSH across the SAF and PF. The mass-loading constituent can, however, exceed 30% of the total signal, such as in the event around October 26, 2008 at site D02 (figure 1.16).

There was less variability and higher amplitude mass-loading signals at site C14 on the southern end of the transport line. The range of SSHA is one-third the size of the sites further north (figure 1.16) due to the more moderate SSH gradients in the region. For most of the record, the mass-loading and steric constituents are of similar magnitude.

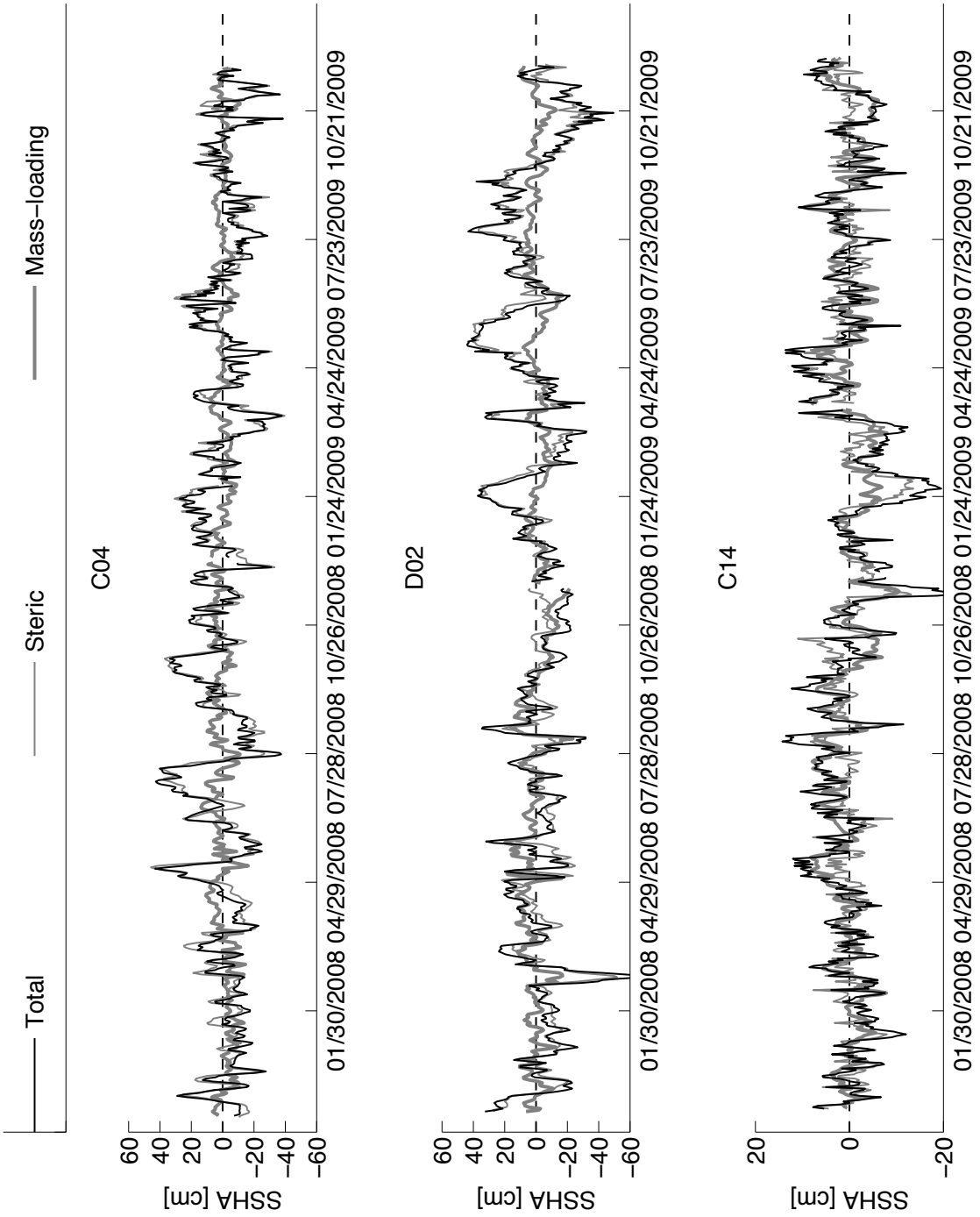


Figure 1.16: Time series of SSHA and its constituents at three sites, with $p_{ref}$ equal to the instrument's depth. Note that the y-axis range is different for site C14, lowest panel.

There were three low SSH events between November 2008 and March 2009. These events are the SACCF meandering over C14.

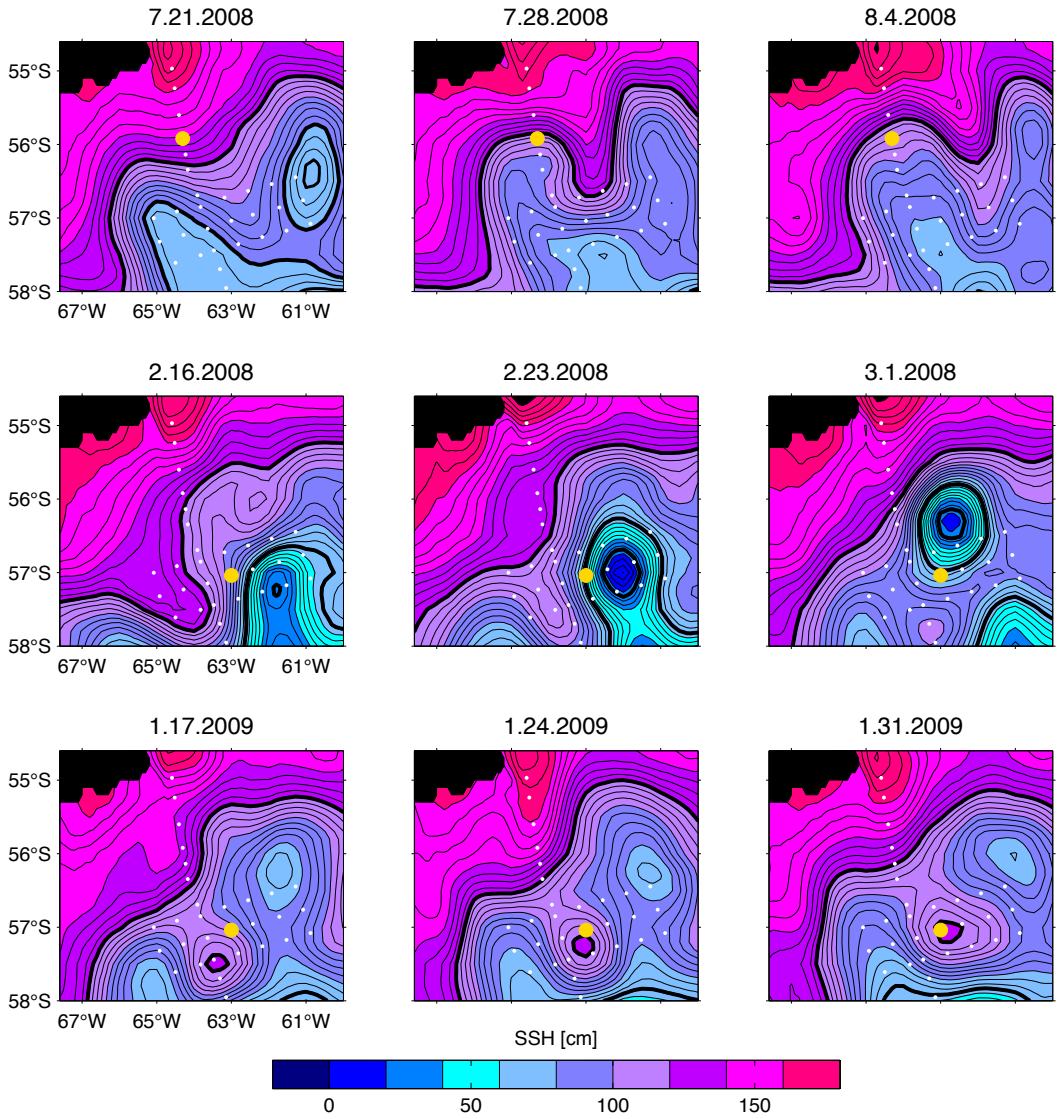


Figure 1.17: Rows show sequences of SSHA events at sites C04 (top) and D02 (middle and bottom). Color-shaded contours are SSH from the Aviso merged product with the RIO05 mean dynamic topography every 20cm, thin black contours have a 5 cm contour interval. A colorbar corresponding to the SSH values is located at the bottom of the figure. The thick black lines are the estimated positions of the SAF (120 cm contour) and the PF (65 cm contour) and their associated eddies. Land is shown in solid black. cDrake sites are marked with white dots. Yellow dots represent the sites corresponding with time series from figure 1.16 that correspond to the depicted event.

The variance at northern sites is dominated by the steric signal while total variance along the southern end of the transport line is split almost equally between the mass-loading and steric constituents. Peak SSHA variance was found within the LDA sites and a drastic decline of total and steric SSHA variance occured south of the Shackleton Fracture Zone (figure 1.18). North of 57°S, steric SSHA variance exceeded 60% of the total SSHA variance. Large mass-loading contribution to SSHA events were often but not always co-varying with the steric component, and this was due to periods of cyclogenesis [*Chereskin et al.*, 2009]. In fact, the site for the LDA was chosen as the region of highest surface EKE with the objective of examining mesoscale processes (figure 1.19). The coupling of the steric and mass-loading constituents during cyclogenesis led to the high covariance values in the LDA. A drastic decline of total and steric SSHA variability occurred south and west of the Shackleton Fracture Zone, at site C10 (inset of figure 1.18). In addition, the partition between mass-loading and steric contributions changed. South of 59°S, the mass-loading SSHA variance exceeded 40% of the total SSHA variance and in places reaches 65% of the total variance. The two constituents are not correlated, however.

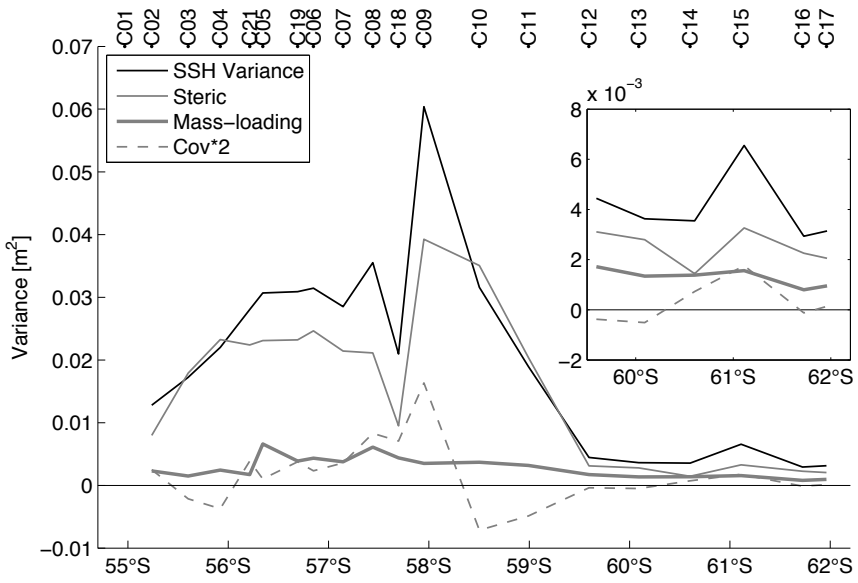


Figure 1.18: Variance of SSHA and its constituents and their covariance along the transport line as a function of latitude. Inset panel is an expanded y-axis for the southern part of the Transport Line, units on y-axis are meters squared.

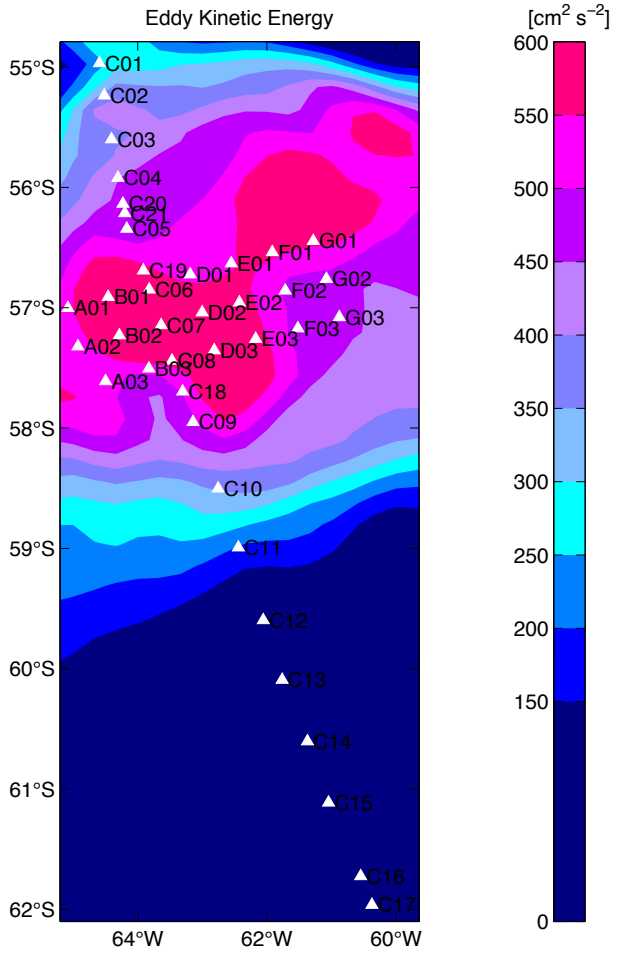


Figure 1.19: Map of surface eddy kinetic energy. Colored contours are 17-year average (14 Oct 1992 to 18 Feb 2009) of surface eddy kinetic energy from altimetry from *Chereskin et al.* [2009]. cDrake sites are shown with white triangles.

The SSHA variance of the cDrake sites in the LDA is comparable with the values found in the South Atlantic Cape Basin in the Agulhas South-Atlantic Thermohaline Transport Experiment (ASTTEX) by *Baker-Yeboah et al.* [2009]. The ASTTEX mass-loading SSHA maximum variance is 25% higher than the maximum from the cDrake array. In the Kuroshio Extension System Study, the total SSHA variance peaked at 0.2 m$^2$ and the mass-loading constituent was much smaller than the cDrake study [*Park*, 2010].

Examining SSHA variance as a function of frequency showed that most energy is at frequencies of 1/20 cpd and lower (figure 1.20). Forty to fifty percent of the energy in

total SSHA north of site C10 was associated with periods longer than 1/20 cpd. South of 58.5°S, periods longer than 20 days only account for 10 to 30%.

Meandering of the three ACC fronts about their mean positions occurred, creating peaks in variance (upper panel of figure 1.21). The SAF meanders can be seen near 56°S, the PF between 57°S and 59°S, and the SACCF between 60°S and 61.5°S. The SAF and PF were of similar strength (0.005 $m^2$) while the SACCF was much smaller (0.0005 $m^2$) which was a reflection of its smaller steric signal.

Mass-loading variance is highest in the region of cyclogenesis and the magnitude at all frequencies in northern Drake Passage is significantly smaller than the steric constituent. Mass-loading spectra (bottom panel of figure 1.21) had increased variability below 0.06 cycles per day, especially between 57°S and 58°S in the LDA. At 61°S, the mass-loading constituent has peaks in energy between 1/10 and 1/20 cpd, whereas the steric constituent peaked at frequencies lower than 1/25 cpd at the same latitude.

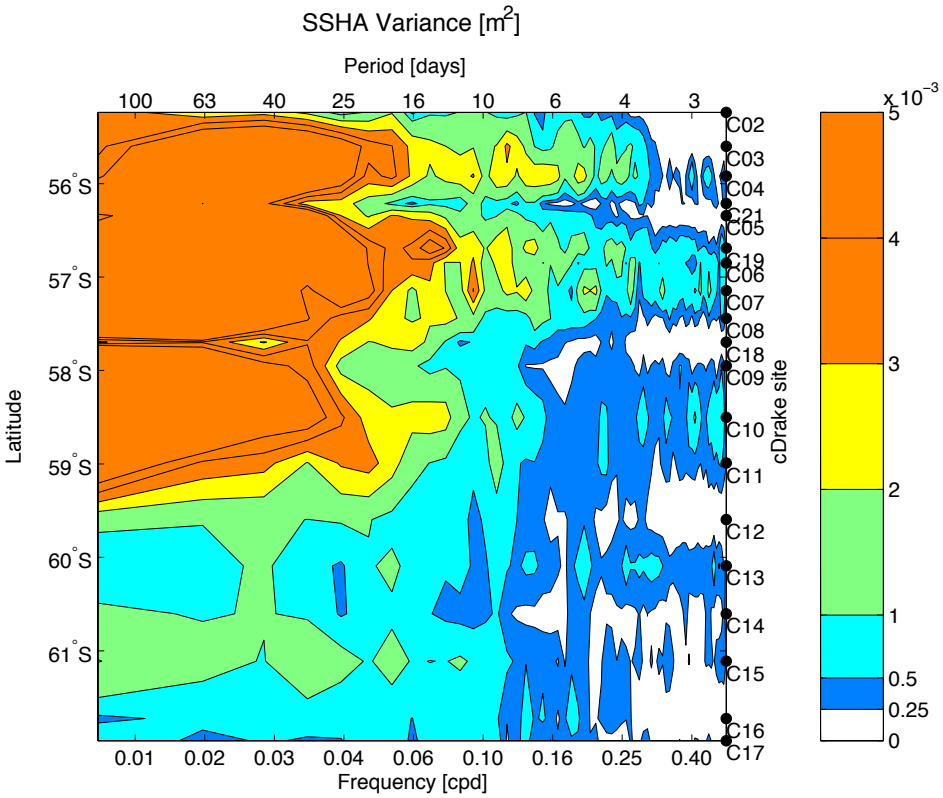


Figure 1.20: Spectral energy of total SSHA as a function of latitude along the transport line and frequency.

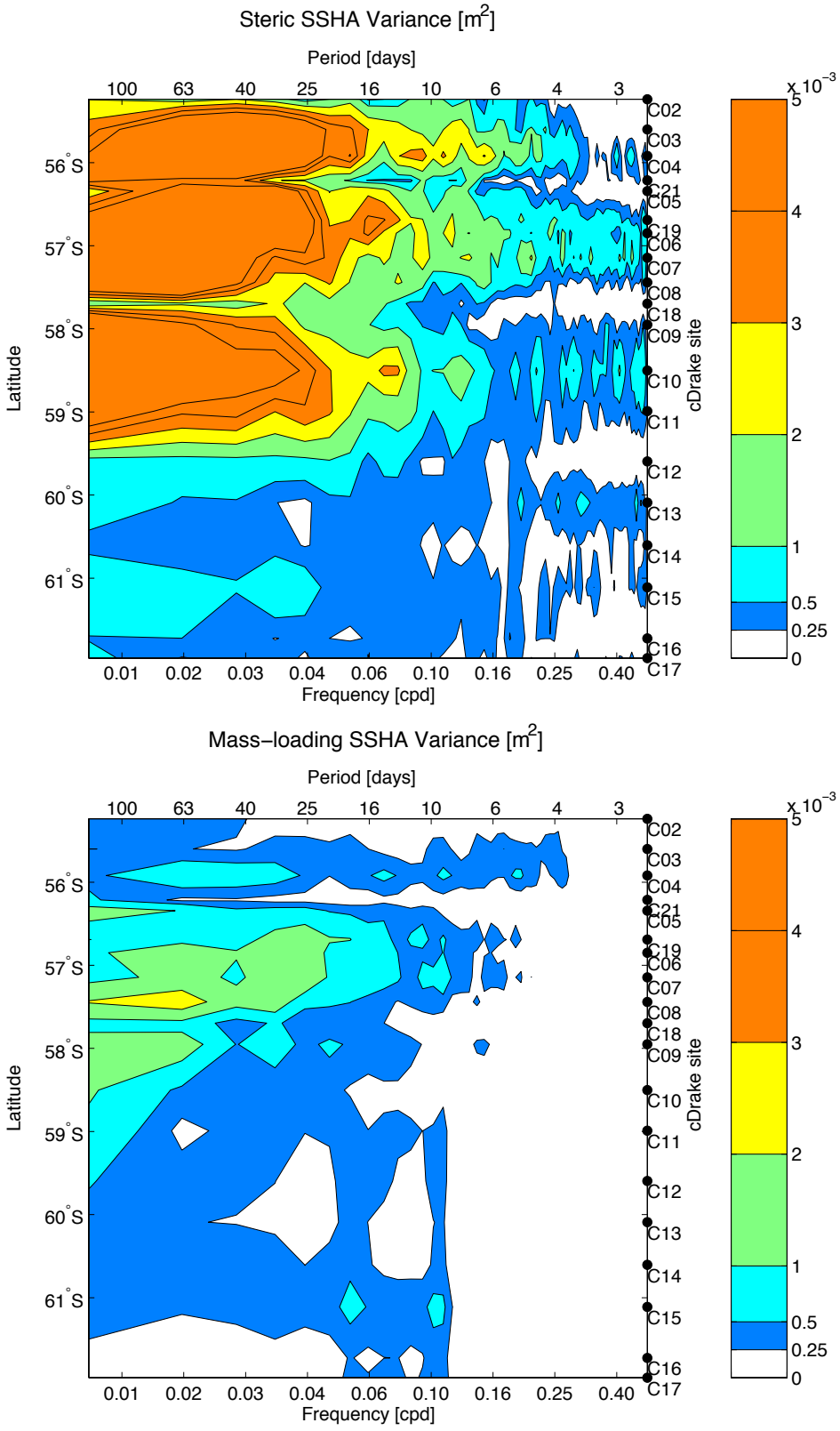


Figure 1.21: Upper (lower) panel is spectral energy of the steric (mass-loading) component of SSHA as a function of latitude along the transport line and frequency.

### 1.4 Aliasing of SSHA

Several oceanic processes affect SSH with periods between a few hours and 20 days, such as tides, atmospherically-driven responses that are mainly barotropic, topographic and shelf wave processes, and a variety of short period eddy variability. If these signals are not adequately resolved by the sampling rate of measurements, the Nyquist theorem shows that energy with periods shorter than twice the sampling period are aliased to different, lower frequencies, making those lower frequencies appear on average more energetic than they actually are. Using hourly records from recovered cDrake instruments, it was possible to see how much energy was aliased by subsampling the data set at the interval of satellite altimeters. The CPIES hourly measurements were subsampled at 10 day intervals, and the spectrum was computed. This process was iterated, offsetting the starting point by 1 data point each time, until the spectrum had been computed for all data points in the 10 day interval. The average of all individual spectra in the set was computed. Figure 1.22 shows the spectra of the hourly measurements of each time series with this averaged subsampled spectra overlaid to show the differences in energy. The elevated energy at low frequencies in the subsampled spectra was the result of aliasing. Note that C12 is plotted with a y-axis that is a factor of 10 smaller than the other 3 sites.

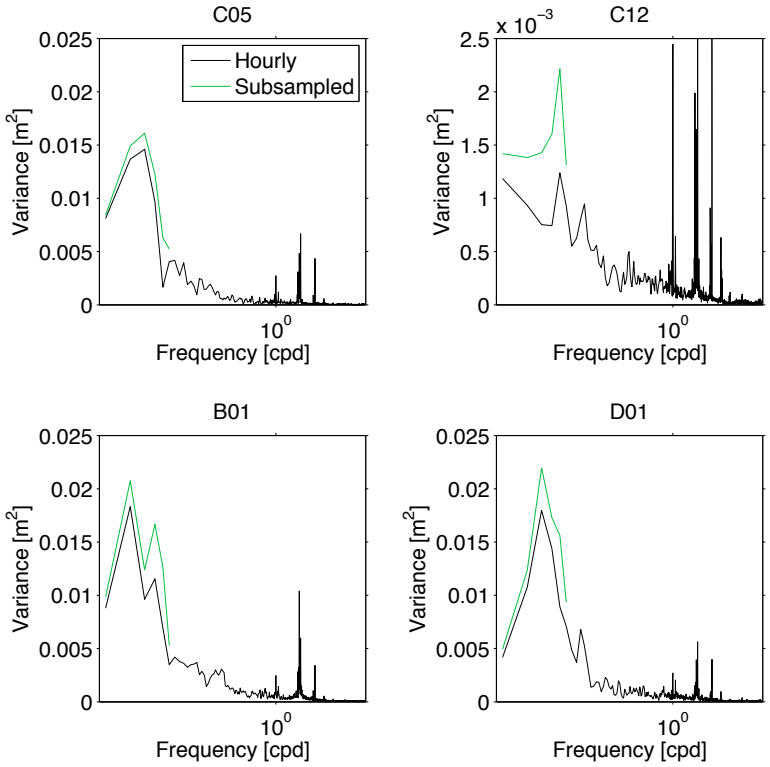


Figure 1.22: Variance of hourly SSHA from the CPIES (black) and subsampled every 10 days (green) as a function of frequency.

The fraction of aliased energy can be quantified at each frequency by calculating

$$R_a = 1 - \frac{E(f)}{E_{subsampled}(f)} \tag{1.10}$$

where $0 < f < 1/20$ cpd [*Gille and Hughes*, 2001]. Negative values occur when not all low-frequency energy is resolved by the subsampling, and zero values indicate perfectly resolved signals. Positive values reveal that high-frequency energy has been aliased to lower frequencies.

Another way to express the amount of aliased energy is in a signal to aliased-signal ratio, reported in dB, similar to how a signal-to-noise ratios are commonly expressed. For this study, the signal to aliased-signal ratio (SAR) is calculated by

$$SAR_{db} = 10log_{10}\left(\frac{E(f)}{E_{subsampled}(f) - E(f)}\right), \tag{1.11}$$

in the same manner as the signal-to-noise ratios (SNR) in *Bendat and Piersol* [2000]. Negative values indicate that there is more aliased energy than energy at that frequency

in the original signal. Zero values indicate equal values of actual and aliased energy, and a value of 6 dB corresponds approximately to $R_a$ of 0.25, or a quarter of the energy is aliased from higher frequencies. Higher values reflect less aliasing. When discussing signal-to-noise ratios in acoustic signal processing, the 6 dB cutoff represents the threshold at which it becomes too difficult to detect the true signal through the noise, and 12 dB is considered a good signal-to-noise ratio to decrease the chance of false detections [*Urick*, 1967]. In the case of the SAR, it represents the value at which the aliasing becomes too strong and the probability of false detection of signals is too high for the data to be considered accurate.

Up to a quarter of the total energy in 10-day sampled SSHA at all frequencies was due to aliasing in Drake Passage. For frequencies lower than 0.02 cpd, $R_a$ values ranged from 0 to 0.4, which indicated that up to 40% of energy at those frequencies had been aliased (figure 1.23). $R_a$ values fell between 0.4 and 0.8 at almost all sites at a frequency of 0.04 (1/25) cpd. This indicated that at 1/25 cpd, more than half of the energy seen in the subsampled time series was actually aliased from high-frequency signals. Higher variance at frequencies between 1/20 and 1/50 cpd were seen along the transport line compared to within the local dynamics array. The same results were seen when expressing the SAR as a function of frequency (figure 1.24). The values above 6 dB at frequencies longer than 1/50 cpd indicate that if the aliased energy were treated as noise, at low frequencies it would be possible to detect the real signals with a moderate chance of false detection. For low frequencies at any sites have SAR above 12 dB, as would have offered reliable interpretation of long-period signals. At all sites and high frequencies less than 0.02 cpd, however, aliasing severely alters the true signals.

Due to the inclusion of steric SSHA in this analysis, these values provide better estimates of the amount of energy aliased by the altimetric products. *Gille and Hughes* [2001] based their $R_a$ values on bottom pressure data with the underlying assumption that bottom pressure variability would be a proxy for sea surface height variability. They found that with a few exceptions, $R_a$ was less than 0.5 for frequencies longer than 1/50

cpd. Results here suggest that the outlook for total SSHA is slightly better in Drake Passage, as the $R_a$ values are less than 0.25 at most sites for lower frequencies.

The steric component of sea surface height showed a similar pattern to the total sea surface height (figure 1.25) in that there was a peak in aliased energy at most sites centered near 1/25 cpd and a quarter of the total energy there was due to aliasing. At 1/100 cpd, there was relatively little aliasing ($R_a < 0.25$) and the subsampled time series more closely determined the true signals at that low frequency. More energy at frequencies higher than 1/30 cpd was aliased than in total SSHA.

The percentage of mass-loading SSHA energy that was aliased was greater than steric SSHA energy. At most sites and frequencies, mass-loading $R_a$ exceeded 0.2 (figure 1.26). The peak that was evident in the total and steric SSHA signals at 1/25 cpd was also seen in the mass-loading constituent. However, for frequencies higher than 1/50 cpd, there was significantly more aliasing in the mass-loading constituent. This resulted in aliased energy accounting for up to 50% of the total energy in the spectra, which is consistent with the findings of *Gille and Hughes* [2001]. This study added many more sites throughout the passage, enabling extension of the results further north, south, and west from the *Gille and Hughes* [2001] sites.

While the percentage of energy aliased was larger for the mass-loading than steric constituent, the total variance in each signal must also be considered. The mass-loading signal was aliased more, but the total energy in the time series at sites in northern Drake Passage was dominated by the steric signal. Therefore, when the steric constituent was more than 2/3 of the total SSHA energy, then most of the aliased energy was due to high-frequency steric signals. This was the case in northern Drake Passage and in the LDA. For the southern end of the transport line, where the mass-loading and steric constituents had similar variance, there was more aliased energy from the mass-loading constituent.

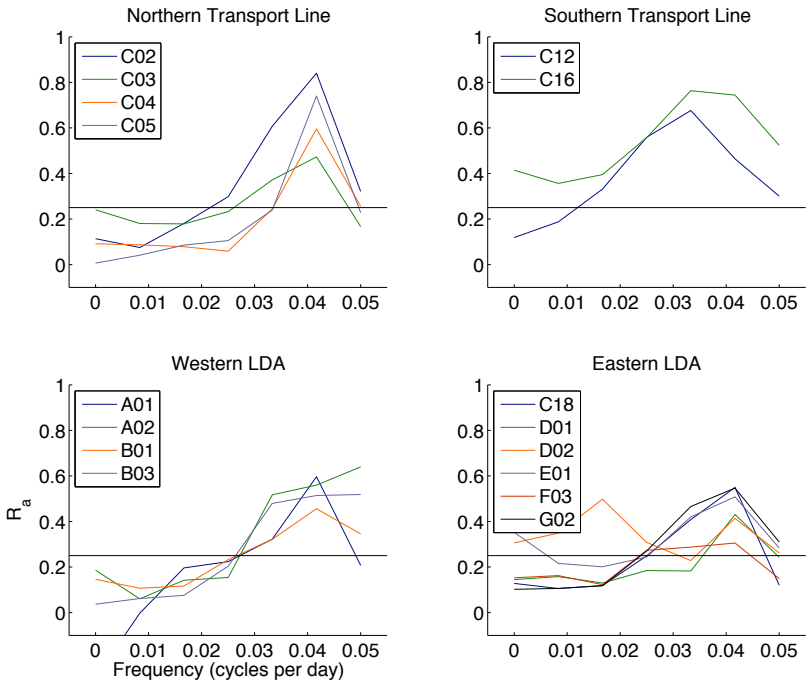


Figure 1.23: Fraction of total sea surface height energy due to aliasing, computed by equation 1.10.

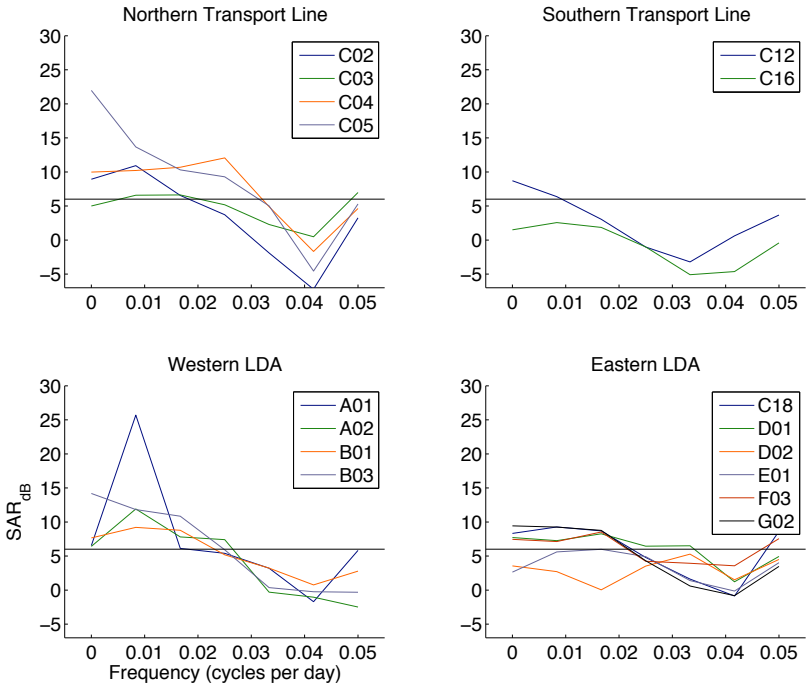


Figure 1.24: Signal to aliased signal ratio in dB for total SSHA, as computed in equation 1.11.

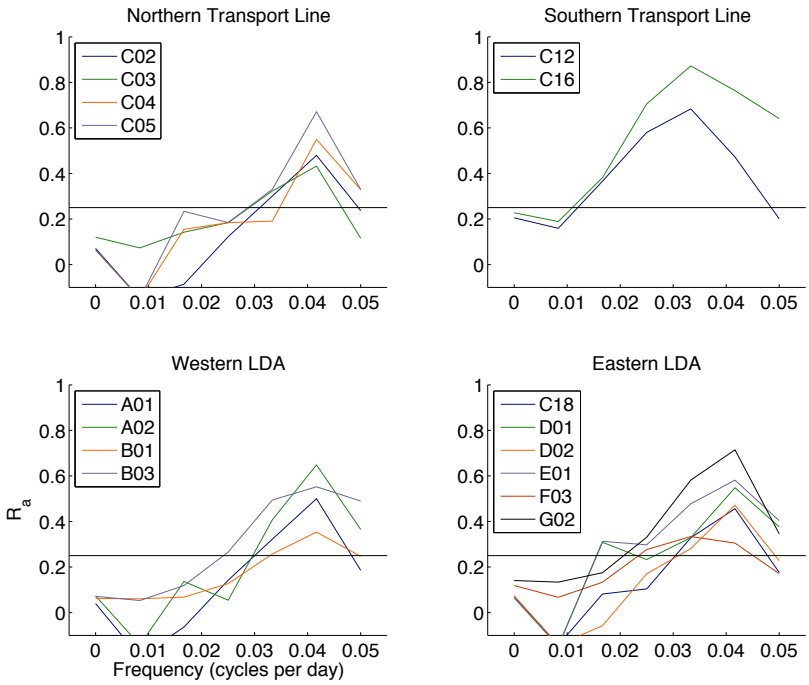


Figure 1.25: Fraction of the steric constituent of sea surface height energy due to aliasing.

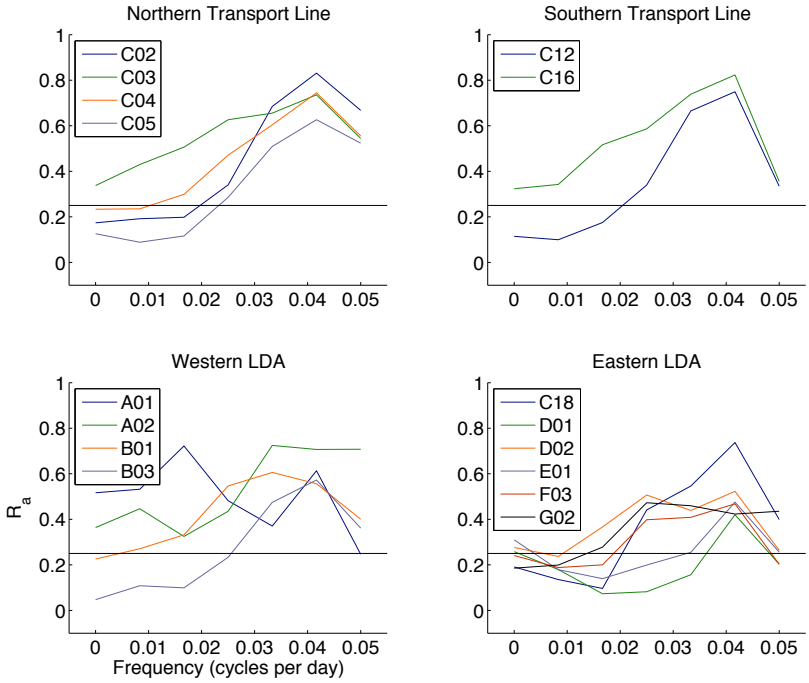


Figure 1.26: Fraction of the mass-loading constituent of sea surface height energy due to aliasing.

## 1.5 Satellite Altimetry Comparisons

### 1.5.1 Along-Track Comparisons

The cDrake transport line was placed along an ERS satellite groundtrack. Due to the presence of a topographic canyon in the continental slope at the northern edge of Drake Passage, C01 through C04 were shifted up to 16 km east of ERS track 351. Fifteen sites were co-located with track 351. The spatial resolution of the ERS satellite in Drake Passage is approximately 40 km between tracks.

Broadly, the comparisons between CPIES-derived SSHA and altimeter SSH were better in northern Drake Passage and within the LDA than those south of the Shackleton Fracture Zone. The three sites, highlighted in figure 1.27, had comparable RMS differences between CPIES and altimeter SSHA near 0.06 m yet the visual correspondence and correlations between the two products varied between these sites. C08 and altimeter compared well; The correlation coefficient between CPIES and altimeter SSHA was 0.93. A linear regression yielded a slope of 1.18, which indicated that the altimeter measurements underestimated the SSHA, however, the slope was not statistically different from 1. The C08 time series illustrates how the 1/35 cpd ERS sampling often missed SSHA signals: the low and two high peaks that occurred between December 2008 and June 2009 were not sampled by the satellite. At site C12, the correlation coefficient between CPIES and altimeter SSHA was 0.65, less than at C08, yet clearly the two time series tracked each other. The large high events between March and September 2008 were both captured by the altimeter. Plots of CPIES versus AVISO showed a slope of only 0.76, but the large uncertainty of the slope again showed the relationship was not statistically different from a slope of 1. In contrast, at C16 on the southern end of the transport line, the correlation coefficient between CPIES and altimeter SSHA was only 0.26. There were not any large-amplitude low-frequency signals as there were in the C08 and C12 records. There were four events between June and September 2008 with an amplitude of 10 cm that the altimeter sampling did not resolve.

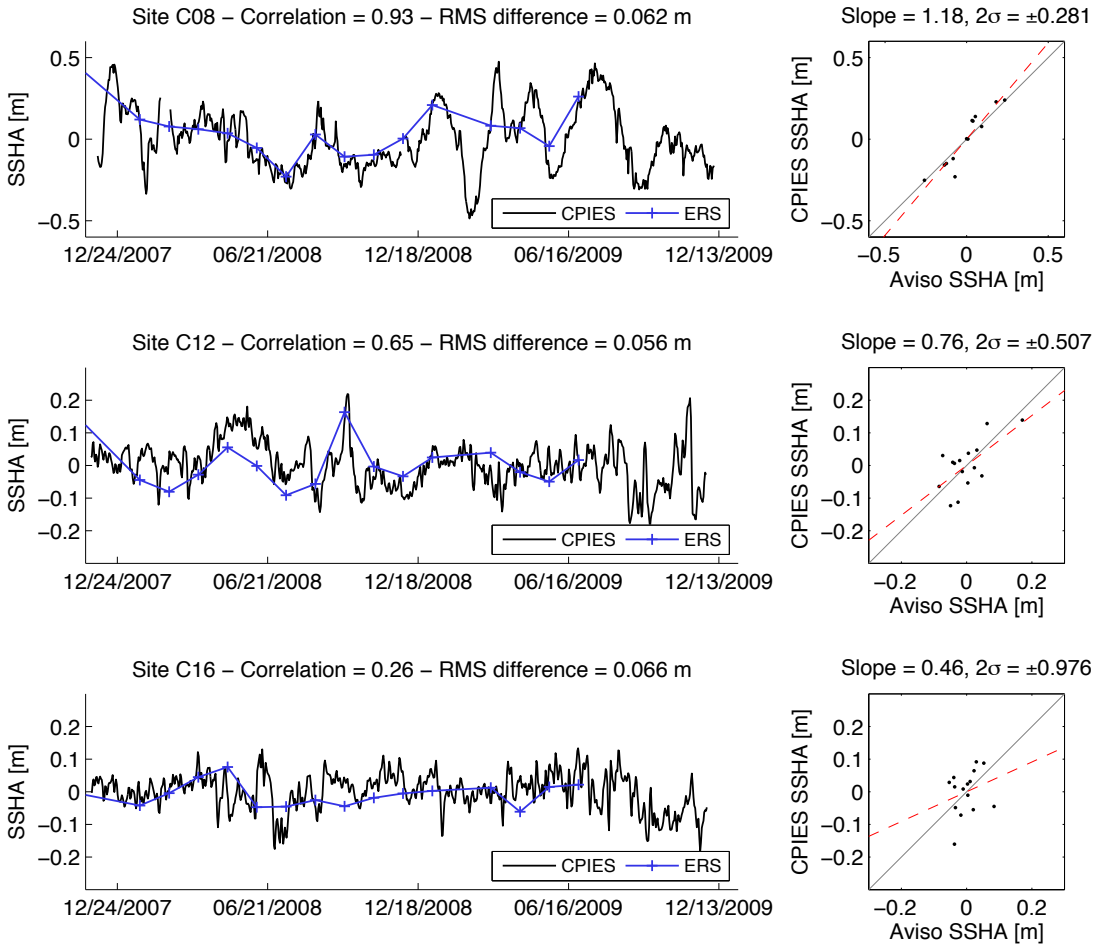


Figure 1.27: The left panels show time series of SSHA from CPIES and AVISO along-track product. The black time series are daily values of SSHA from 3 CPIES sites along the cDrake transport line coincident with ERS groundtracks. The blue crosshairs are the measurements from the ERS satellite. Correlation and RMS difference is listed in each plot title. The panels on the right are the CPIES values plotted against the AVISO values (black dots), a linear fit (dashed red) with slope and 95% confidence interval of the slope noted in the title, and the 1:1 ratio (gray line).

There was strong latitudinal dependence of both correlation and variability in the cDrake and AVISO SSHA products (figure 1.28). The correlations were high when the recorded variance was high. Sites with RMS signal greater than 0.15 m had correlations greater than 0.9. These sites with high signal and correlations were all north of the Shackleton Fracture Zone (58.5°S). Note that the RMS for the ERS and CPIES is actually a standard deviation since each time series has zero mean. The southern end of the transport line was much less variable and the signal to noise ratio was close to 1. The error in Aviso's along-track product is 3.4 cm [*Aviso*, 2008] and the RMS of the ERS measurements at sites C16 and C17 was only 3.7 cm. The error estimate from spectral analysis of the CPIES data showed that in the southern end of the transport line, the error is 3.5 cm, which was also close to the RMS value of the CPIES measurements. This accounts for lower correlation coefficients there.

The determination of the statistical significance of the correlation coefficients depends upon the effective degrees of freedom. The integral time scale for Drake Passage was found to be 30 days from autocorrelation functions as in *Emery and Thompson* [2001]. The effective degrees of freedom ($N^*$) is

$$N^* = \frac{N\Delta t}{T} \tag{1.12}$$

where $N$ is the number of measurements, $\Delta t$ is the frequency of measurements, and $T$ is the integral time scale. Because ERS sampling at 35 days was longer than this 30 day time scale, the effective degrees of freedom for timeseries used in the ERS-CPIES comparison equalled the number of measurements (table 1.5). With 13 degrees of freedom, a correlation coefficient of 0.514 is statistically significant at the 95% confidence level. Only 2 sites (C11 and C16) did not meet this criteria [*Emery and Thompson*, 2001].

There are several possible reasons for low correlations between the CPIES and altimeter measurements of SSHA. First, the distance between the two estimates was as great as 9.5 km (Table 1.5) because the CPIES were compared to the closest standard-grid point measurement along the altimeter track. Small spatial or temporal scale disturbances could have caused discrepancies between the two. Secondly, the altimetry

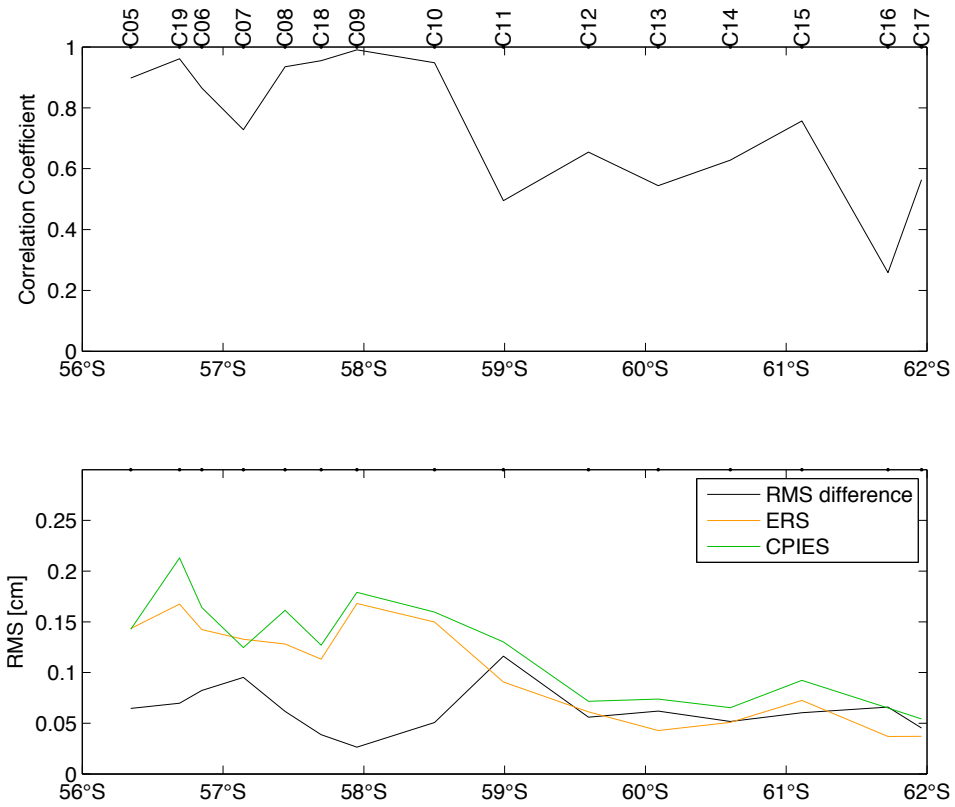


Figure 1.28: Top panel is the correlation coefficient between AVISO's along-track ERS product and CPIES SSHA at sites along the transport line plotted as a function of latitude. The lower panel is the RMS of each signal, also as a function of latitude.

product processing could have introduced differences between the data sets. Processing included some smoothing along the track and a barotropic high-frequency correction. The smoothing is unlikely to impact the southern sites much since the correlation length scales are so long there. The high-frequency correction needs improvement, which is discussed in greater detail in section 1.5.3. Finally, error could be introduced by weather and ice conditions. Increased sea surface roughness due to storms impact both the $\tau$ measurements and the altimetry measurements. Sites far south, such as C16 and C17, may be affected by sea ice in the austral winter months which would impact the altimetry and CPIES measurements.

| **Site** | **Correlation** | **Dist from site [km]** | **RMS ERS [m]** | **RMS CPIES [m]** | **RMS difference [m]** | **# points** |
|---|---|---|---|---|---|---|
| C05 | 0.90 | 5.2 | 0.143 | 0.143 | 0.065 | 10 |
| C06 | 0.87 | 5.7 | 0.142 | 0.164 | 0.082 | 15 |
| C07 | 0.73 | 9.5 | 0.133 | 0.125 | 0.095 | 15 |
| C08 | 0.93 | 4.7 | 0.128 | 0.161 | 0.062 | 13 |
| C09 | 0.99 | 5.7 | 0.168 | 0.179 | 0.026 | 5 |
| C10 | 0.95 | 7.9 | 0.150 | 0.160 | 0.051 | 14 |
| C11 | 0.49 | 9.3 | 0.091 | 0.130 | 0.116 | 13 |
| C12 | 0.65 | 3.1 | 0.061 | 0.072 | 0.056 | 15 |
| C13 | 0.54 | 1.8 | 0.043 | 0.074 | 0.062 | 14 |
| C14 | 0.63 | 3.4 | 0.051 | 0.065 | 0.052 | 14 |
| C15 | 0.76 | 4.1 | 0.073 | 0.092 | 0.060 | 13 |
| C16 | 0.26 | 1.8 | 0.037 | 0.065 | 0.066 | 15 |
| C17 | 0.56 | 6.6 | 0.037 | 0.054 | 0.045 | 15 |
| C18 | 0.95 | 4.5 | 0.113 | 0.127 | 0.039 | 10 |
| C19 | 0.96 | 4.4 | 0.168 | 0.213 | 0.070 | 14 |

Table 1.5: Correlations between cDrake CPIES SSHA and AVISO's along-track ERS satellite product. ERS data is from the closest point along the track to the CPIES site. The distance between the ERS measurement and the CPIES site is in column four. RMS of CPIES is computed with only the measurements on days with an ERS measurement.

### 1.5.2 Merged-Product Comparisons

In addition to the along-track data from the altimeters, Aviso produces a merged product that combines both the ERS and Jason satellites to produce a gridded product every 7 days. While most cDrake sites did not lie on a Jason satellite line, the addition of those tracks to the merged product enabled weekly comparisons between every cDrake site and the mapped product. For this analysis, the merged product with $1/3^\circ$ grid was interpolated to each CPIES site.

The sites highlighted in the ERS along-track comparisons (figure 1.27) are repeated using the mapped SSHA records (figure 1.29). At the site with highest variance, C08 displayed the same high correlation of 0.93 with the merged as the along-track product. The addition of the neighboring ERS tracks and Jason satellite data enabled it to resolve the large signals that the along-track data missed during the beginning of 2009. Site C12, however, correlated worse with the merged product, dipping from a correlation coefficient of 0.65 to 0.436. Its low variance and large distance to Jason groundtracks likely made it susceptible to errors in the mapping process. Site C16 did not correlate with either Aviso product.

The addition of the Jason satellite data and the mapping yielded a product that resolved many more events than the ERS observations did alone. To illustrate this, figure 1.30 shows the time series at a cDrake site on the northern transport line, the middle of the LDA, and on the southern transport line. At sites C04 and D02, the product resolved the large and low-frequency events well, although for several events it underestimated the change in SSHA. At site C14, a major event in January 2009 was completely missed. Overall, however, more of the signal is resolved with the merged product.

Three sites along the A-line are presented (figure 1.31) because they have similar characteristics yet different juxtapositions relative to altimeter tracks. Site A01 was on both an ERS and Jason groundtrack, and close to a crossover point in both satellites orbit paths. A02 was situated on the same ERS line as A01, but at a greater distance to any Jason track. Site A03 was placed east of the ERS path to avoid a seamount. The

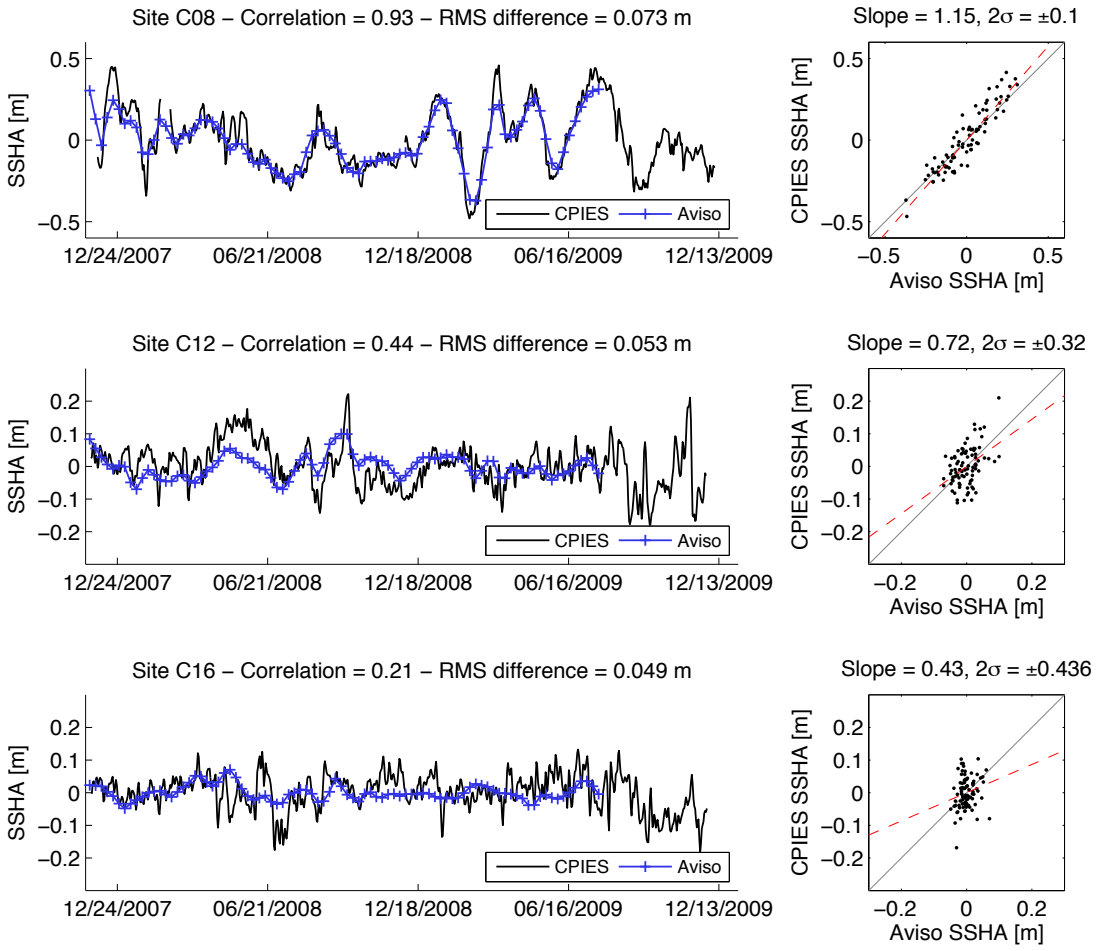


Figure 1.29: The left panels show time series of SSHA from CPIES and AVISO merged, gridded product. The black time series are daily values of SSHA from 3 CPIES sites along the cDrake transport line coincident with ERS groundtracks that were also shown in the comparison with the ERS along-track data. The blue crosshairs are the measurements from the Aviso product. Correlation and RMS difference is listed in each plot title. The panels on the right are the CPIES values plotted against the AVISO values (black dots), a linear fit (dashed red) with slope and 95% confidence interval of the slope noted in the title, and the 1:1 ratio (gray line).

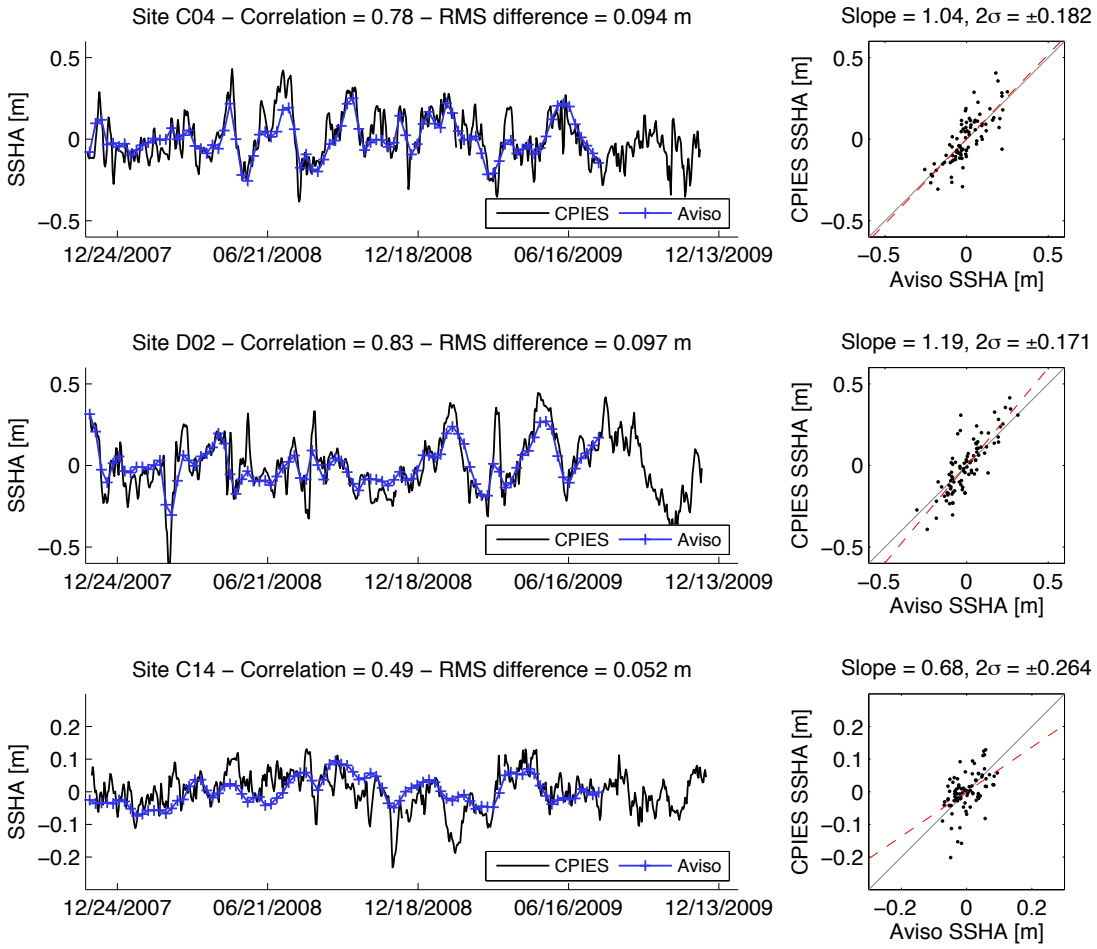


Figure 1.30: The left panels show time series of SSHA from CPIES and AVISO merged, gridded product. The black time series are daily values of SSHA from 3 CPIES sites along the cDrake transport line coincident with ERS groundtracks. The blue crosshairs are the measurements from the Aviso product. Correlation and RMS difference is listed in each plot title. The panels on the right are the CPIES values plotted against the AVISO values (black dots), a linear fit (dashed red) with slope and 95% confidence interval of the slope noted in the title, and the 1:1 ratio (gray line).

best correlation would be expected from A01 due to its proximity to so many altimetric measurements, however A02 actually agreed best with a correlation coefficient of 0.904, which was 0.03 higher than at site A01. The AVISO merged product underestimated the amplitude of signals by about 20%: the RMS of the Aviso product was smaller than the CPIES subsampled at the same weekly interval, and the slope of the linear fit in the right panels of figure 1.31 was greater and statistically different than 1. In addition to smoothing introduced by the AVISO processing, this underestimation may also be due to the mapping procedure used to create the merged product. Low-frequency, long-wavenumber signals dominate in the LDA, which allowed for the good correlations in this region regardless of distance to satellite tracks.

The RMS of the merged product along the transport line was lower at most sites than the ERS altimeter alone. However, correlations were similar and the latitudinal dependence was still apparent, as shown in figure 1.32. Overall the correlations were good, especially in the northern transport line and LDA. The majority of sites had correlations above 0.8. The effective degrees of freedom for the correlations with the merged altimetry measurements is approximately 18 for most cDrake sites, as not all measurements are independent. With 18 degrees of freedom, a correlation coefficient of 0.444 is statistically significant at the 95% confidence level, and only 3 sites (C12, C13, and C16) did not meet this criteria [*Emery and Thompson*, 2001].

The errors in the Aviso merged product were a combination of the 3.4 cm error in the along-track products and the error in the mapping process, bringing the total error to 4.5 cm at times. Examples of mapping errors and total errors in relation to time series are shown in section 1.2.6. The variable error may have contributed to the differences in amplitude of eddies in their mapped products, which led to the RMS differences between the CPIES data and the merged Aviso product. The altimeters will not perform as well in areas where there are small spatial features or rapidly propagating features. These signals would not be well-resolved by the individual altimeters, and therefore difficult to map accurately.

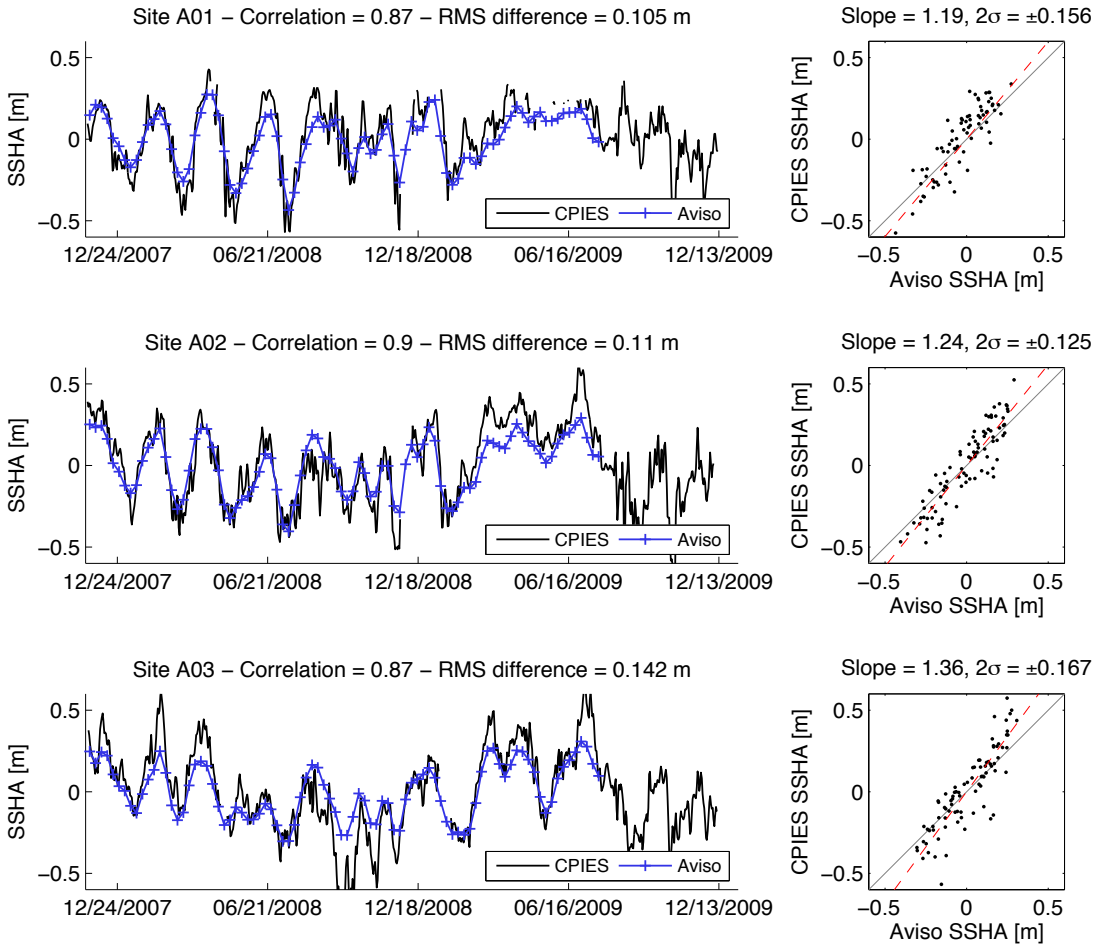


Figure 1.31: The left panels show time series of SSHA from CPIES and AVISO merged, gridded product. The black time series are daily values of SSHA from 3 CPIES sites along the cDrake transport line coincident with ERS groundtracks. The blue crosshairs are the measurements from the Aviso product. Correlation and RMS difference is listed in each plot title. The panels on the right are the CPIES values plotted against the AVISO values (black dots), a linear fit (dashed red) with slope and 95% confidence interval of the slope noted in the title, and the 1:1 ratio (gray line).

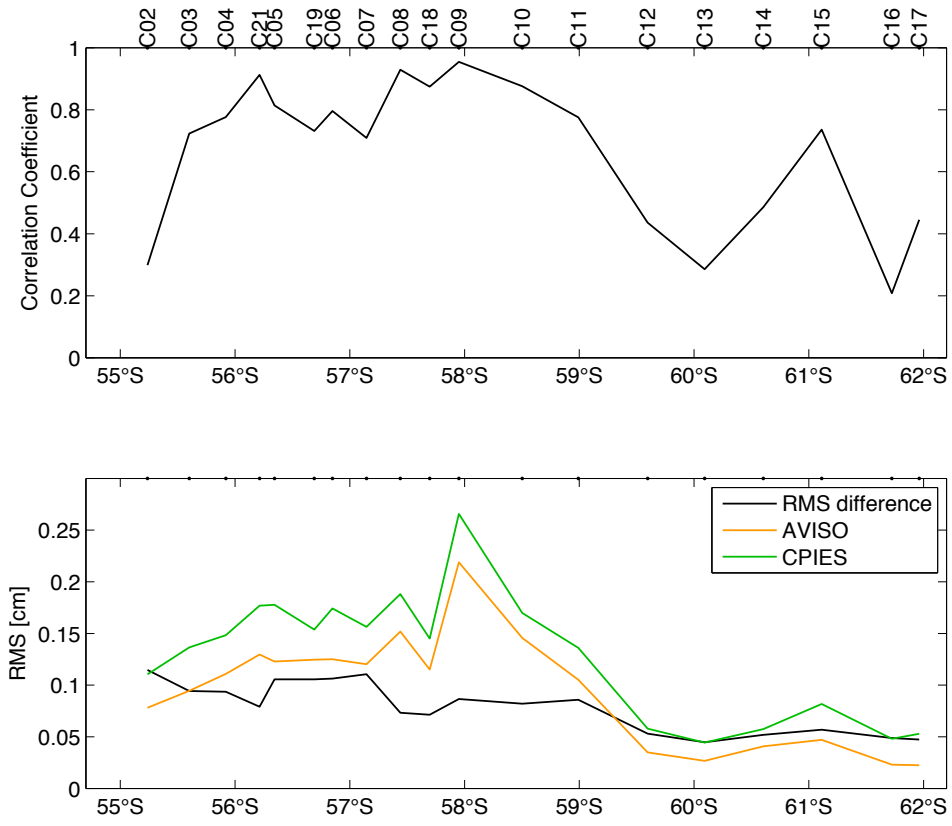


Figure 1.32: Top panel is the correlation coefficient between AVISO's merged, gridded product and CPIES SSHA at sites along the transport line plotted as a function of latitude. The lower panel is the RMS of each signal, also as a function of latitude.

Table 1.6: Correlations between cDrake CPIES SSHA and AVISO's merged satellite product.

| Site | Correlation | RMS of AVISO | RMS of CPIES | RMS difference | # pts |
|---|---|---|---|---|---|
| A01 | 0.874 | 0.152 | 0.208 | 0.105 | 73 |
| A02 | 0.904 | 0.174 | 0.238 | 0.110 | 87 |
| A03 | 0.870 | 0.168 | 0.262 | 0.142 | 85 |
| B01 | 0.829 | 0.142 | 0.190 | 0.107 | 88 |
| B02 | 0.820 | 0.147 | 0.249 | 0.154 | 86 |
| B03 | 0.832 | 0.166 | 0.216 | 0.121 | 88 |
| C02 | 0.299 | 0.078 | 0.110 | 0.115 | 50 |
| C03 | 0.723 | 0.094 | 0.136 | 0.094 | 88 |
| C04 | 0.776 | 0.111 | 0.148 | 0.094 | 86 |
| C05 | 0.814 | 0.123 | 0.178 | 0.106 | 55 |
| C06 | 0.796 | 0.125 | 0.174 | 0.106 | 88 |
| C07 | 0.709 | 0.120 | 0.156 | 0.111 | 86 |
| C08 | 0.929 | 0.152 | 0.188 | 0.073 | 85 |
| C09 | 0.954 | 0.219 | 0.266 | 0.087 | 33 |
| C10 | 0.876 | 0.146 | 0.170 | 0.082 | 84 |
| C11 | 0.776 | 0.105 | 0.136 | 0.086 | 83 |
| C12 | 0.436 | 0.035 | 0.058 | 0.053 | 87 |
| C13 | 0.286 | 0.027 | 0.044 | 0.045 | 87 |
| C14 | 0.485 | 0.041 | 0.057 | 0.052 | 87 |
| C15 | 0.736 | 0.047 | 0.082 | 0.057 | 87 |
| C16 | 0.208 | 0.023 | 0.048 | 0.049 | 87 |
| C17 | 0.445 | 0.022 | 0.053 | 0.047 | 86 |
| C18 | 0.875 | 0.115 | 0.145 | 0.071 | 54 |
| C19 | 0.732 | 0.125 | 0.154 | 0.106 | 86 |
| C21 | 0.912 | 0.130 | 0.177 | 0.079 | 32 |
| D01 | 0.656 | 0.131 | 0.158 | 0.122 | 87 |
| D02 | 0.830 | 0.118 | 0.169 | 0.097 | 88 |
| D03 | 0.898 | 0.127 | 0.167 | 0.077 | 87 |
| E01 | 0.767 | 0.153 | 0.156 | 0.105 | 86 |
| E02 | 0.461 | 0.126 | 0.156 | 0.149 | 86 |
| E03 | 0.880 | 0.135 | 0.184 | 0.091 | 87 |
| F01 | 0.870 | 0.157 | 0.173 | 0.085 | 87 |
| F02 | 0.739 | 0.144 | 0.145 | 0.104 | 75 |
| F03 | 0.836 | 0.138 | 0.173 | 0.095 | 88 |
| G01 | 0.741 | 0.161 | 0.213 | 0.143 | 76 |
| G02 | 0.799 | 0.117 | 0.141 | 0.085 | 88 |
| G03 | 0.784 | 0.104 | 0.137 | 0.085 | 86 |

### 1.5.3 High-Frequency Corrections to Altimetry

Aviso is constantly trying to improve its processing schemes and corrections to reduce SSHA errors. Spectral analysis of CPIES-derived SSHA showed variability at frequencies higher than 1/20 cpd. The sampling rate of the altimeters will alias this high-frequency variability. To reduce this aliasing, AVISO applies a dynamic atmosphere correction (DAC). Unfortunately, AVISO does not save the Mog2D-G output offline but rather bundles the HF and IB corrections and delivers this as a product. Because the IB and HF corrections contain signals within the same frequency range it is impossible to isolate the two corrections. AVISO does separate the corrections in their along-track Topex, Jason-1 and Jason-2 geophysical data records. Therefore both the IB and HF corrections are available at 1/20 cpd resolution.

Two recovered instruments coincided with Jason groundtracks, one within the LDA (A01) and one just south of the LDA (C09). The comparison between these LDA measurements and the HF correction is not likely to be favorable in this region because LDA mass-laoding SSHA is strongly influenced by cyclogenesis. The DAC records were compared with the mass-loading constituent of SSHA from the CPIES after being high-pass filtered with a 20-day cut-off (4th order Butterworth filter). Site A01 showed no correlation. Site C09 had a correlation coefficient of 0.78 (table 1.7). The RMS of the Aviso records were both around 1.3 cm, while the CPIES at site A01 (C09) were 8.27 (2.20) cm (table 1.7). The RMS difference was large, especially at A01 where the variance in the CPIES record was very high.

| | **AVISO [cm]** | **CPIES [cm]** | **RMS difference [cm]** | **Correlation** |
|---|---|---|---|---|
| **A01** | 1.35 | 8.29 | 8.32 | 0.06 |
| **C09** | 1.28 | 3.00 | 2.20 | 0.78 |

Table 1.7: RMS of the high frequency signals of the AVISO model correction and the high-pass filtered CPIES mass-loading SSHA, their RMS difference, and correlation.

To look at the pattern of RMS of the DAC across the entire cDrake array, the along-track high-frequency barotropic model outputs from July 2008 through April 2010 were mapped (left panel of figure 1.35). This showed a similar spatial pattern and range in

the passage as the global map published on the AVISO website (figure 1.34). RMS of the 20-day high-pass filtered CPIES measurements from recovered instruments (center panel of figure 1.35) showed the spatial patterns are quite different. The model is much weaker everywhere in Drake Passage and this disagreement was most pronounced in the LDA and northern Drake Passage. The 3-day low-pass filtered telemetered data at every cDrake site (right panel of figure 1.35) were utilized to see more of the spatial pattern in the cDrake array. The variance for these records was lower than the hourly records from the recovered instruments because of the averaging and filtering that went into the telemetered records. The variance more closely agreed with the HF correction, which showed that the model was underestimating the high-frequency mass-loading signals everywhere in Drake Passage. The disagreement within the LDA could be anticipated by recognizing that this variability is tied to instabilities within the baroclinic ACC jets. It is also possible that smaller-horizontal scale boundary waves that have a bottom pressure expression might not be resolved by the barotropic model.

The DAC also currently makes no effort to remove high-frequency signals in the steric SSHA. There were high-frequency steric signals that were aliased to frequencies resolved by the altimeters (section 1.3). The signal is of the same magnitude as the mass-loading signal, and should therefore be addressed or accounted for in the error of the altimetry measurements. *Pascual et al.* [2008] suggested the use of the Hindcast of Dynamic Processes of the Ocean and Coastal Areas of Europe (HIOPCAS) model to correct altimetry when there should be a separation between steric and mass contributions. Without an accurate model to correct for these steric signals, the aliased variance must be accounted for in the error budget of the satellite altimeters.

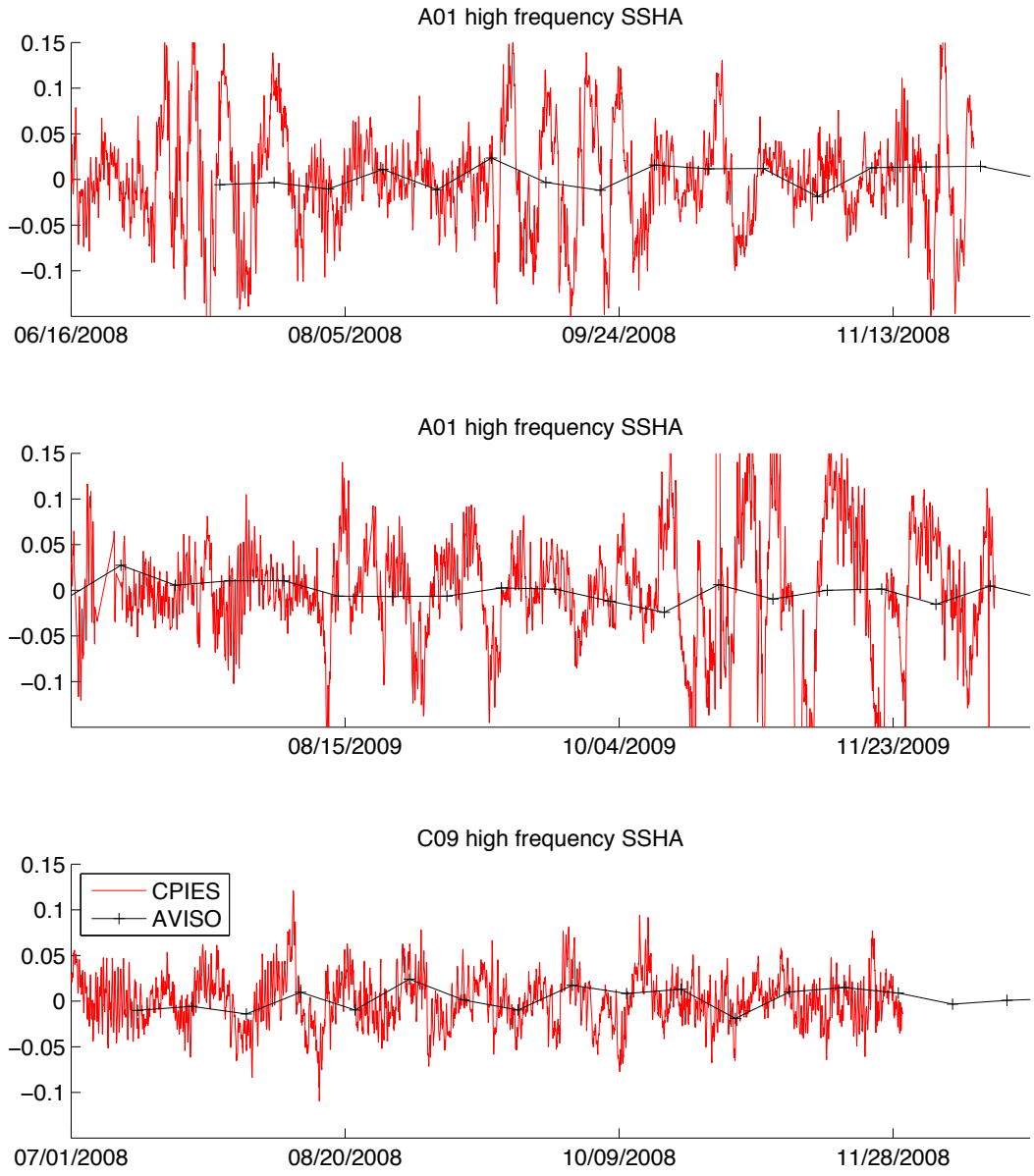


Figure 1.33: Time series of mass-loading SSHA from recovered CPIES instruments, high-pass filtered with a 20 day cutoff shown in red and the AVISO high frequency signal from the Mog2D-G model in black. The upper and middle panels are different time periods at site A01. Lower panel is site C09.

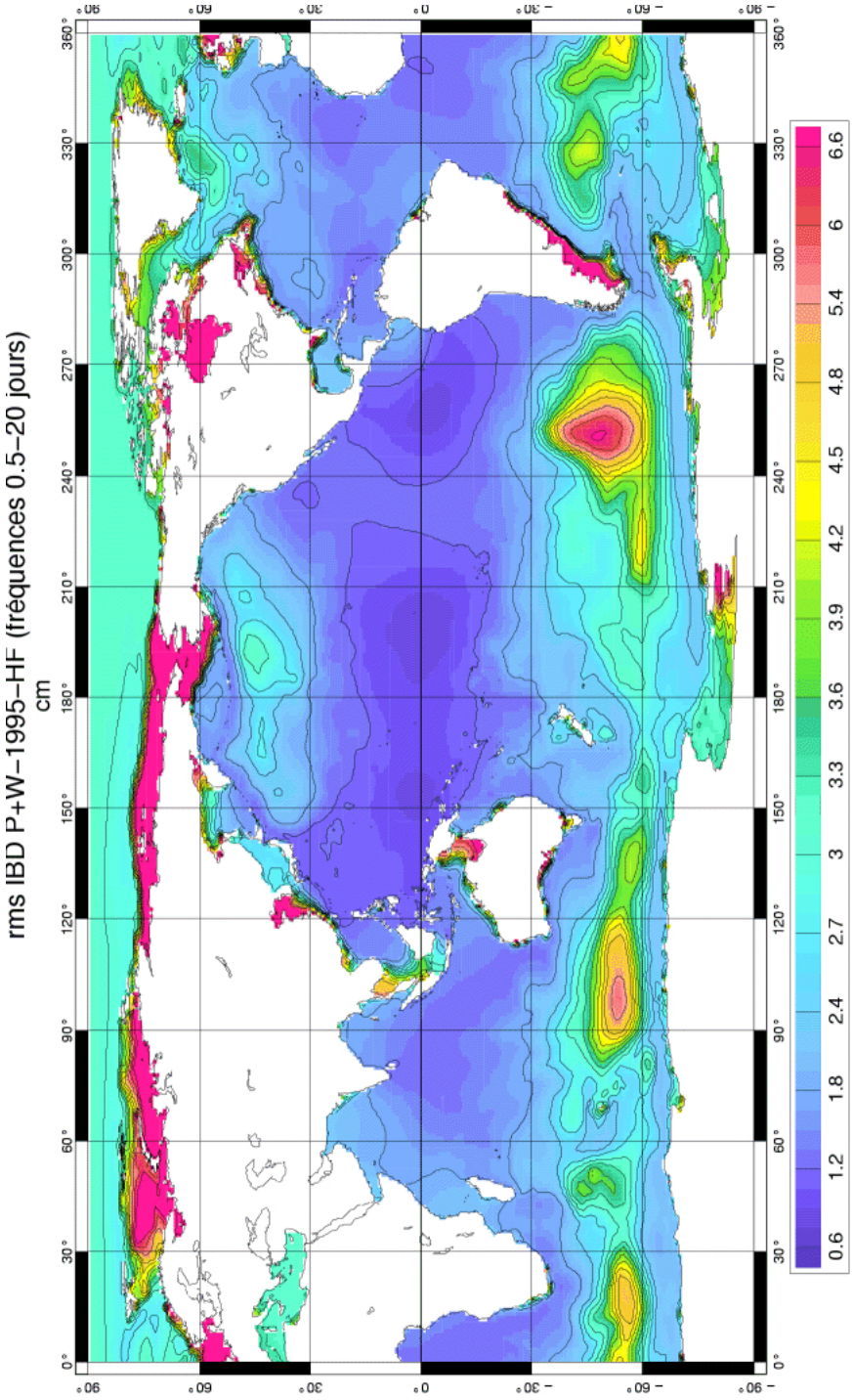


Figure 1.34: Variability of the ocean dynamic response (in cm) due to pressure and winds, from shallow water hydrodynamic model Mog2D. (Credits CLS/Legos, http://www.aviso.oceanobs.com/fileadmin/images/data/Products/auxiliaires/rms_ibd_pv.gif).

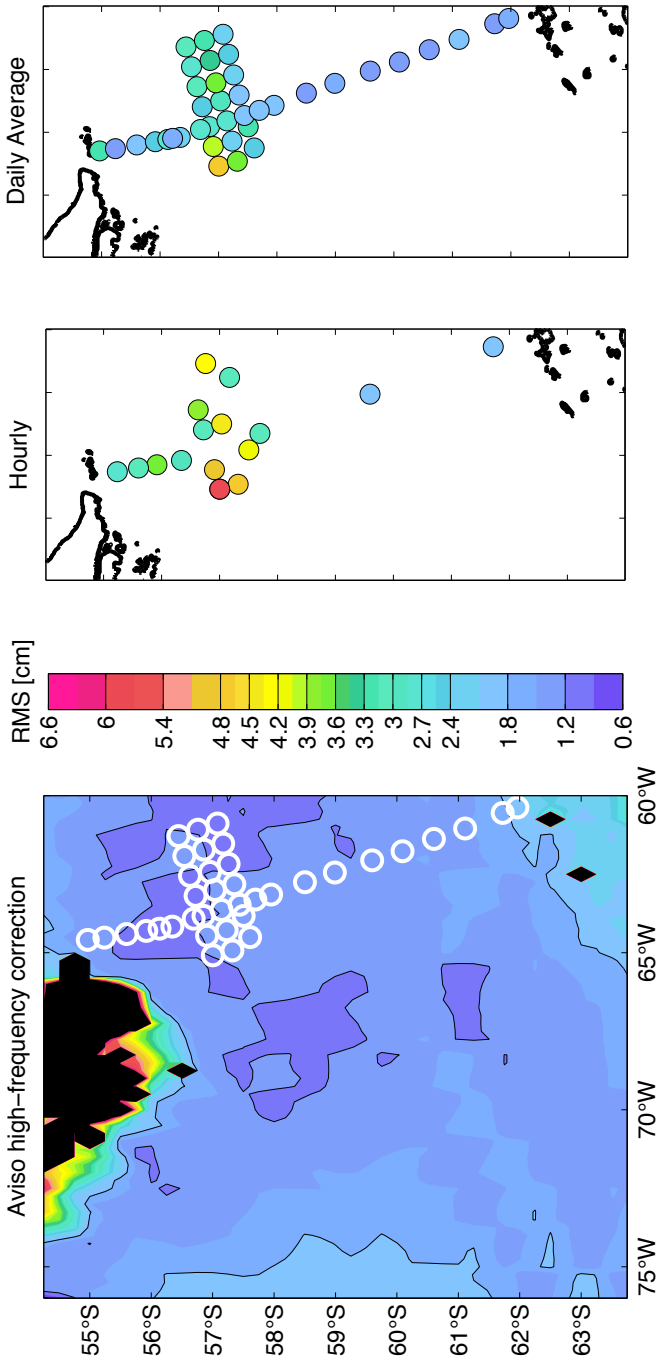


Figure 1.35: Left panel is the RMS of the publicly available high-frequency correction from the Aviso dynamic atmospheric correction for the Jason groundtracks. The colorbar for all plots is shown to the right. The center (right) panel is the RMS value of high-pass filtered cDrake hourly (low-pass filtered daily) CPIES mass-loading SSHA at each site.

## 1.6 Conclusion

The cDrake project has provided an unprecedented dataset to analyze SSHA. Both the steric and mass-loading constituents of SSHA contributed to the total SSHA signal. Steric signals dominated SSHA north of 58.5°S but were of the same order of magnitude as the mass-loading signal along the southern transport line. In northern Drake Passage, however, the mass-loading signal was influential during cyclogenesis and eddy events.

The agreements between the CPIES array and the satellite altimetry products were generally favorable in regions of high SSHA variance. In these regions, the mapped satellite SSHA compared well to CPIES SSHA regardless of distance to a satellite track because in these regions, variability was dominated by low-frequency long-wavenumber signals that were well resolved by the altimeter sampling.

Both constituents have high-frequency signals that the hourly and daily CPIES measurements resolved. For frequencies between 1/50 and 1/20 cpd, between 25% and 75% of the total SSHA energy measured by the altimeter is due to aliasing of higher frequency signals. These high percentages indicate that if satellite measurements were left uncorrected for high-frequency signals, there would be a large error introduced into the altimetric measurements at those frequencies. This work refines the conclusion of *Gille and Hughes* [2001] who only considered the mass-loading component of SSHA. The AVISO corrections for high-frequency signals (above the 1/20 cpd Nyquist frequency of the Jason-1 and Jason-2 satellites) are made with a barotropic model. The model did not correlate well with the CPIES mass-loading high-frequency signals. Furthermore, the AVISO correction does attempt to correct for high-frequency steric signals. The aliasing of higher frequency signals remains a significant problem and improvements to processing procedures will be necessary if satellites are to be the basis of future monitoring efforts in Drake Passage.

## BIBLIOGRAPHY


Aviso (2008), *AVISO and PODAAC User Handbook*.

Aviso (2010), *SSALTO/DUACS User Handbook*.

Baker-Yeboah, S., D. R. Watts, and D. A. Byrne (2009), Measurements of sea surface height variability in the eastern South Atlantic from pressure sensor-equipped inverted echo sounders: Baroclinic and barotropic components, *J. Atmos. Oceanic Tech.*, (doi:10.1175/2009JTECHO659.1).

Bendat, J. S., and A. G. Piersol (2000), *Random Data Analysis and Measurement Procedures*, third ed., Wiley Interscience.

Bingham, R. J., and C. W. Hughes (2008), The relationship between sea-level and bottom pressure variability in an eddy permitting ocean model, *Geophys. Res. Lett.*, *35*, L03,602.

Böning, C. W., A. Dispert, M. Visbeck, S. R. Rintoul, and F. U. Schwarzkopf (2008), The response of the Antarctic Circumpolar Current to recent climate change, *Nature Geoscience*, *1*, 864–869.

Carrere, L., and F. Lyard (2003), Modeling the barotropic response of the global ocean to atmospheric wind and pressure forcing - comparisons with observations, *Geophys. Res. Lett.*, *30*(6), 1275.

Chereskin, T. K., K. A. Donohue, D. R. Watts, K. L. Tracey, Y. Firing, and A. L. Cutting (2009), Strong bottom currents and cyclogenesis in Drake Passage, *Geophys. Res. Lett.*, *36*, L23,602.

deSzoeke, R. A., and M. D. Levine (1981), The advective flux of heat by mean geostrophic motions in the Southern Ocean, *Deep Sea Research*, *28*, 1057–1085.

Donohue, K. A., D. R. Watts, K. L. Tracey, A. D. Greene, and M. Kennelly (2010), Mapping circulation in the Kuroshio Extension with an array of Current and Pressure recording Inverted Echo Sounders, *J. Atmos. Oceanic Tech.*, (doi:10.1175/2009JTECHO686.1).

Emery, W. J., and R. E. Thompson (2001), *Data Analysis Methods in Physical Oceanography*, 2 ed., Elsevier Science Ltd.

Gille, S. T. (2002), Warming of the Southern Ocean since the 1950s, *Science*, *295*, 1275–1277.

Gille, S. T. (2008), Decadal-scale temperature trends in the southern hemisphere ocean, *Journal of Climate*, *21*, 4749–4765.

Gille, S. T., and C. W. Hughes (2001), Aliasing of high-frequency variability by altimetry: Evaluation from bottom pressure recorders, *Geophys. Res. Lett.*, *28*(9), 1755–1758.

Gnanadesikan, A., and R. Hallberg (2000), On the relationship of the Circumpolar Current to Southern Hemisphere winds in coarse-resolution ocean models, *Journal of Physical Oceanography*, *30*, 2013–2034.

Hogg, A. M., M. P. Meredith, J. R. Blundell, and C. Wilson (2007), Eddy heat flux in the Southern Ocean: Response to variable wind forcing, *Journal of Climate*, *21*, 608–620.

Jayne, S. R., J. M. Wahr, and F. O. Bryan (2003), Observing ocean heat content using satellite gravity and altimetry, *J. Geophys. Res.*, *108*(C2), 3031–3042.

Lenn, Y.-D., T. K. Chereskin, and J. Sprintall (2008), Improving estimates of the Antarctic Circumpolar Current streamlines in Drake Passage, *Journal of Physical Oceanography*, *38*, 1000–1010.

Meinen, C. S., and D. R. Watts (2000), Vertical structure and transport on a transect

across the North Atlantic Current near 42N: Time series and mean, *J. Geophys. Res.*, *105*, 21,869–21,891.

Munk, W. H., and D. E. Cartwright (1966), Tidal spectroscopy and prediction, *Philosophical Transactions of the Royal Society A*, *259*, 533–581.

Orsi, A. H., T. W. Whitworth, and W. D. N. Jr (1995), On the meridional extent and fronts of the Antarctic Circumpolar Current, *Deep Sea Research*, *42*, 641–673.

OSU (2009), The OSU TOPEX/Poseidon Global Inverse Solution TPXO Version 7.1, *http://www.coas.oregonstate.edu/research/po/research/tide/global.html*.

Park, J.-H. (2010), Sea surface height variability in the Kuroshio Extension, personal communication.

Pascual, A., M. Marcos, and D. Gomis (2008), Comparing the sea level response to pressure and wind forcing of two barotropic models: Validation with tide gauge and altimetry data, *Journal of Geophysical Research*, *113*, C07,011.

Smith, W. H. F., and D. T. Sandwell (1997), Global seafloor topography from satellite altimetry and ship depth soundings, *Science*, *277*, 1957–1962.

Speer, K. G., S. R. Rintoul, and B. M. Sloyan (2000), The diabatic Deacon cell, *Journal of Physical Oceanography*, *30*, 3212–3222.

Sun, C., and D. R. Watts (2001), A circumpolar gravest empirical mode for the Southern Ocean hydrography, *Journal of Geophysical Research*, *106*(C2), 2833–2855.

Urick, R. J. (1967), *Principles of Underwater Sound for Engineers*, McGraw-Hill.

Volkov, D. L., G. Larnicol, and J. Dorandeu (2007), Improving the quality of satellite altimetry data over continental shelves, *Journal of Geophysical Research*, *112*, C06,020.

Watts, D. R., C. Sun, and S. R. Rintoul (2001), A two-dimensional gravest empirical mode determined from hydrographic observations in the Subantarctic Front, *J. Phys. Oceanogr.*, *31*, 2186–2209.

Whitworth, T. (1983), Monitoring the net transport of the Antarctic Circumpolar Current at Drake Passage, *Journal of Physical Oceanography*, *13*, 2045–2057.

Whitworth, T., and R. G. Peterson (1985), The volume transport of the Antarctic Circumpolar Current from three-year bottom pressure measurements, *Journal of Physical Oceanography*, *15*, 810–816.

Yang, X.-Y., R. Z. Huang, and D. X. Wang (2007), Decadal changes of wind stress over the Southern Ocean associated with Antarctic ozone depletion, *Journal of Climate*, *20*, 3395–3410.